International Reviews in Physical Chemistry, 2013
Vol. 32, No. 1, 128–170, http://dx.doi.org/10.1080/0144235X.2012.752904

New mass spectrometry techniques for studying physical chemistry of atmospheric heterogeneous processes

Julia Laskin[a]*, Alexander Laskin[b] and Sergey A. Nizkorodov[c]

[a]*Chemical and Materials Sciences Division, Pacific Northwest National Laboratory, Richland, WA 99352, USA;* [b]*Environmental Molecular Sciences Laboratory, Pacific Northwest National Laboratory, Richland, WA 99352, USA;* [c]*Department of Chemistry, University of California, Irvine, CA 92697, USA*

(*Received 14 September 2012; final version received 21 November 2012*)

Ambient particles and droplets have a significant effect on climate, visibility and human health. Once formed, they undergo continuous transformations through condensation and evaporation of water, uptake of low-volatility organic molecules and photochemical reactions involving various gaseous and condensed-phase species in the atmosphere. These transformations determine the physical and chemical properties of airborne particles, such as their ability to absorb and scatter solar radiation and nucleate cloud droplets. The complexity, heterogeneity and size of ambient particles make it challenging to understand the kinetics and mechanisms of their formation and chemical transformations. Mass spectrometry (MS) is a powerful analytical technique that enables detailed chemical characterisation of both small and large molecules in complex matrices. This capability makes MS a promising tool for studying chemical transformations of particles and droplets in the atmosphere. This review is focused on new and emerging experimental MS-based approaches for understanding the kinetics and mechanisms of such transformations. Some of the techniques discussed herein are best suited for ambient samples, while the others work best in laboratory applications. However, in combination, they provide a comprehensive arsenal of methods for characterisation of particles and droplets. In addition, we emphasise the role of fundamental physical chemistry studies in the development of new methods for chemical analysis of ambient particles and droplets.

Keywords: mass spectrometry; ambient particles; ambient droplets; reaction kinetics and mechanisms; depth profiling

Contents

*Corresponding author. Email: julia.laskin@pnnl.gov

1. Introduction

Ambient particles are complex mixtures that often contain both organic and inorganic components. The components may be uniformly distributed within particles, forming an internally mixed aerosol, or separated from each other, forming an externally mixed aerosol. Furthermore, various components in a given particle often separate into domains with different phase states, for example, a solid inorganic core fully or partially engulfed by a liquid organic phase [1,2]. Chemical reactivity of such complex systems is a strong function of their size, morphology, chemical composition and surface properties. Reactions taking place on surfaces of ambient particles are increasingly believed to play an important role in atmospheric chemistry [3]. For example, reactive uptake of hydroxyl radicals (OH) and ozone (O_3) may lead to oxidation of the surface organics, thereby altering a particle's hygroscopic properties [4]. Photochemical reactions involving surface-active photosensitisers may lead to unconventional oxidation of volatile organic compounds (VOCs), such as isoprene, causing secondary organic aerosol (SOA) formation [5]. Because the sizes of atmospheric particles vary from several nanometers for freshly nucleated particles to several hundred nanometers for accumulation-mode particles to several microns for mechanically generated particles, studying their physicochemical properties with a single analytical method is especially challenging. Therefore, a variety of complementary analytical approaches have been developed for both bulk and single-particle characterisation of ambient particles [6,7].

Aqueous droplets found in clouds and fogs are generally larger than particles, typically ranging from a fraction of a micrometer to several millimeters in diameter. The distinction between a 'particle' and a 'droplet' is a matter of semantics. In this review, the term 'particles' will refer to atmospheric particulates with a relatively small fraction of water, and 'droplets' will denote particulates that are almost entirely aqueous. Although they are dominated by water, droplets also contain a number of dissolved organic and inorganic components, as well as suspended insoluble particulates, bioorganism debris and even living organisms [9]. Fogs tend to contain smaller droplets with significantly larger concentrations of the solutes, especially in urban areas [10]. The air–water interface separating the surrounding gas phase and the droplet's interior represents a unique environment, which not only serves as a gateway to the gas-droplet exchange but also promotes chemical processes that do not occur in the bulk environment [11,12]. For example, there is significant experimental evidence of SOA formation and ageing

occurring in the aqueous atmospheric droplets [13]. In addition, the organic solutes, especially the amphiphilic and non-polar organic compounds, are significantly enhanced at the droplet surface [14]. The size of the air–water interface, equivalent to just several molecular layers, and its highly dynamic nature places significant demands on the selectivity and sensitivity of the methods required to probe this delicate environment.

Mass spectrometry (MS) is uniquely suited for comprehensive molecular characterisation of complex systems. The complexity of atmospheric particles and their wide size distribution presents a significant challenge for MS analysis on a particle-by-particle basis. Nevertheless, MS has been widely used for both online characterisation of ambient particles and droplets and offline analysis of particles collected on substrates and bulk samples of cloud and fog waters. The analytical performance and numerous applications of these techniques have been extensively reviewed [15–27] and will not be discussed in this review article. Instead, we will focus on the role of MS in studying physical chemistry of ambient particles and droplets with a special emphasis placed on characterisation of their surface properties.

The advent of ambient surface ionisation techniques [28–33] that enable direct analysis of aerosol samples collected on substrates has opened up new opportunities for studying the mechanisms and reactivity of organic aerosols (OA). Although these techniques have been developed for applications in biology and forensics, they have been recently used for characterisation of the composition and reactivity of atmospheric aerosols. Examples include applications of high-resolution mass spectrometry (HR-MS) coupled to desorption electrospray ionisation (DESI) [34], nanospray desorption electrospray ionisation (nano-DESI) [35], atmospheric solid analysis probe (ASAP)-MS [36], extractive electrospray ionisation (EESI) [37] and liquid extraction surface analysis [38].

A number of other exciting new developments in the MS of droplets have made it possible to selectively probe the processes occurring at the air–water interface. These methods take advantage of the fact that ions produced from surface-active species in charged or highly polarised droplets naturally originate from the droplet surface. This review will highlight three especially promising droplet MS methods: (1) field-induced droplet ionisation MS (FIDI-MS) [39,40], (2) MS of microjets [41] and (3) charge-assisted laser desorption/ionisation (CALDI) [42], in which surface chemistry is probed using either electrospray or laser-based ionisation techniques. An alternative approach to probing surface properties in droplets is to reduce the droplet size to several nanometers. The fraction of surface-bound molecules in droplets of such small sizes becomes comparable to that of bulk molecules. The caveat to this approach is that the chemical composition of the surface also changes with the particle size as a result of the Kelvin effect and increased competition for the surfaces sites. Furthermore, molecular-level effects become important as the droplet size is pushed into the domain of large molecular clusters. We will highlight several novel applications of ion-mobility spectrometry (IMS) coupled in tandem with MS to study the properties of nanodroplets.

Despite significant advancements in soft ionisation MS techniques, their sensitivity is still insufficient for studying chemical transformations of complex particles on a single-particle basis. In contrast, MS approaches that generate ions through laser ablation (LA) or bombardment of surfaces using energetic primary ion beams demonstrate great potential for single-particle analysis [43]. However, the energetic interrogation of surfaces results in facile fragmentation of molecules, which presents a significant challenge for understanding and interpreting the experimental data. For example, LA coupled with MS is commonly used for the elemental analysis of surfaces [44]. However, because LA is a non-linear process, a fundamental understanding

of physicochemical phenomena accompanying laser–surface interactions [45] is essential for the development of improved quantification using this technique. In addition, depth profiling of particles and surfaces using LA relies on reproducible formation and the shape of the crater formed during laser irradiation [46]. Similar challenges are associated with understanding and controlling ion formation through sputtering [47].

In this review, we will describe new and emerging MS techniques for studying the kinetics and mechanisms of chemical transformations of ambient particles and droplets in the atmosphere. In the future, these techniques may provide understanding of the effect of particle heterogeneity on the kinetics and mechanisms of gas-to-particle reactions in the atmosphere. The review is organised as follows. First, we introduce ambient surface ionisation techniques suitable for bulk characterisation of particles collected on substrates. Next, we describe recent developments in MS-based surface analysis techniques for chemical analysis of individual particles on surfaces. In the last section, we discuss new MS approaches for studying chemistry on surfaces of liquid droplets and nanodroplets. This review is by no means exhaustive. Rather, it complements several excellent recent reviews [15–26] describing figures of merit and analytical applications of more traditional MS-based techniques for on- and off-line aerosols analysis.

2. Chemical analysis of substrate-deposited particles and surfaces

2.1. *Ambient surface ionisation techniques*

Over the last few years, a large group of ambient surface ionisation MS techniques have been developed for chemical characterisation of organic and biological analytes on surfaces [28]. These techniques enable rapid and sensitive detection of substrate-deposited molecules without sample pre-treatment and, therefore, offer a unique opportunity for studying physical chemistry of substrate-bound particles and environmental surfaces. Physical principles of close to 30 variations of ambient surface ionisation techniques and their applications have been extensively reviewed [28–30,33,48–51]. Their distinguished features are defined by specific designs of the corresponding ambient surface sampling/ionisation sources that use common ionisation principles, such as electrospray, photoionisation, plasma and chemical ionisation. Understanding environmental effects of aerosols, their sources, formation and atmospheric chemistry relies on a fundamental knowledge of the relationship between their molecular composition and their chemical and physical properties. Ambient surface ionisation techniques produce molecular ions without significant fragmentation and are ideally suited for studying chemical transformations of organic molecules resulting from physicochemical processes pertinent to atmospheric ageing of aerosols. While many of these techniques can be used for characterisation of particles collected on substrates, we will focus only on methods that have been used for studying physical and chemical transformations of ambient particles relevant to understanding their atmospheric chemistry.

Figure 1(a) illustrates DESI MS – the first and, arguably, most established ambient surface ionisation technique – introduced by Cooks and co-workers in 2004 [52]. In this technique, simultaneous sampling and ionisation of analyte molecules take place when charged electrospray droplets impact a sample positioned in close proximity to a mass spectrometer inlet. Analyte desorption in DESI is typically attributed to a ‘droplet pickup’ process [28,53], in which the initial wetting of the sample and dissolution of analyte is followed by a subsequent release of secondary charged droplets containing solvated analyte molecules [54–56]. In

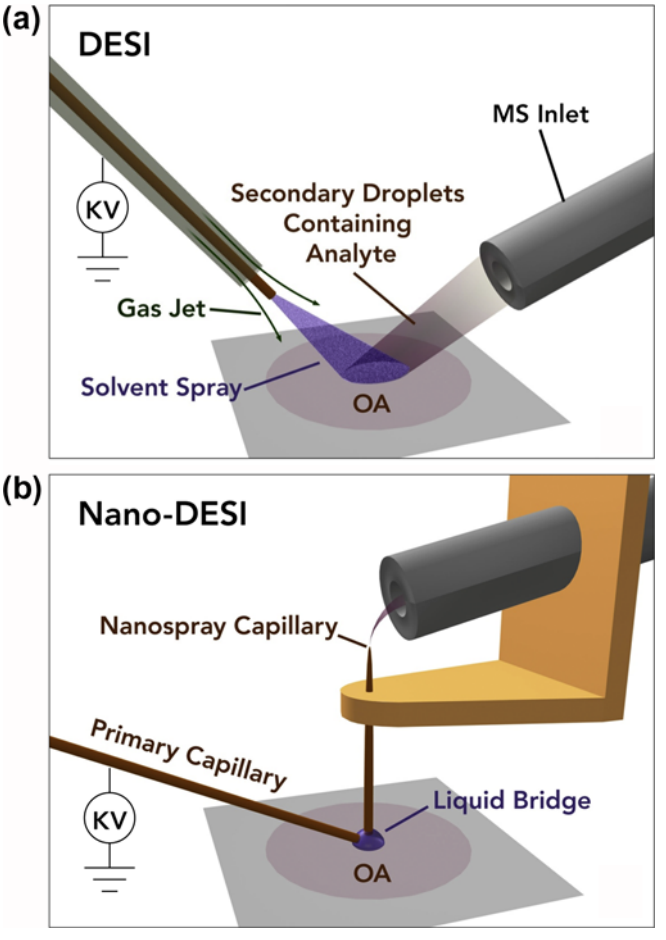

Figure 1. (Colour online) Schematic drawings of two ambient surface ionisation techniques used for the analysis of OA samples: (a) DESI and (b) nano-DESI. Reproduced with permission from Ref. [18].

a typical DESI experiment, a nebulising gas (e.g. nitrogen) accelerates the incoming droplets and provides the necessary momentum to the secondary droplets for their transfer to a mass spectrometer inlet. In addition to the 'droplet pickup' mechanism, an indirect ionisation process has been recently described by Wood *et al.* [57]. Specifically, in that study, the 'droplet pickup' mechanism was suppressed by placing a physical barrier between the spray tip and mass spectrometer inlet. Despite the presence of the barrier, they observed analyte signal in a mass spectrometer. Microscopy imaging indicated that the ion signal was produced from Taylor cones formed at the ends of charged rivulets streaming away from the impact area. Depending on the source geometry and the sample's position with respect to the mass spectrometer inlet, ionisation through 'charged rivulets' formed at a distance from the impact area can become the only mechanism responsible for the DESI signal [57]. As such, the presence of 'charged rivulets' is detrimental to the technique's performance because it results in transport of the analyte on the substrate. Furthermore, the formation of the secondary

charged droplets from the rivulets is a poorly controlled process that reduces the efficiency of the analyte transfer to the mass spectrometer inlet, hence reducing the sensitivity and the stability of the MS signal.

More efficient transfer of the dissolved analyte can be accomplished by placing a self-aspirating capillary between the sample and the instrument. This approach is used in a nano-DESI source [35] shown schematically in Figure 1(b). In nano-DESI, analyte molecules are desorbed into a solvent bridge formed between two glass capillaries brought into close proximity to a solid or liquid sample. The primary capillary delivers a solvent to the surface, while the secondary nanospray capillary removes the solvent and transfers it to a mass spectrometer inlet. When a field gradient is created at the mass spectrometer inlet, a Taylor cone is formed at the tip of the secondary capillary, resulting in nanospray ionisation of the dissolved analyte. The primary capillary supplies solvent at a flow rate adjusted to maintain the liquid bridge and provide stable source operation. This approach separates desorption and ionisation processes and offers improved sampling efficiency and signal stability [35]. In addition, the size of the probed area under the liquid bridge can be precisely controlled for chemical imaging applications [58]. Similar to ESI [59], positive ion mode DESI and nano-DESI result in the formation of protonated molecules $[M+H]^+$ and molecules cationised on metals, such as sodium $[M+Na]^+$ adducts, while deprotonated $[M-H]^-$ molecules are observed in the negative ion mode.

The unique traits of DESI and other ambient surface ionisation MS techniques that enable analysis of substrate-deposited analytes without sample preparation have resulted in widespread applications, including analysis of pharmaceutical compounds, biological samples, forensics, explosives, crude oil, polymers, fragrances and other complex analytes [30–33,50,60]. Recently, DESI and nano-DESI have been used for understanding physical chemistry of atmospheric aerosols and their molecular-level reaction chemistry [34,61–70]. Traditional methods of collecting airborne particles in field and laboratory studies by filtering and impaction are ideally suited for subsequent analyses using ambient surface ionisation approaches. However, thus far, relatively few ambient surface ionisation techniques have been used for chemical analysis of collected aerosol particles. These studies (discussed herein) demonstrate the power of ambient surface ionisation MS techniques for understanding the physical chemistry of ambient aerosols. When coupled with HR-MS, these techniques enable accurate mass measurements for both abundant and minor peaks in the spectrum and structural characterisation of the major peaks using MS^n experiments. For example, Roach *et al.* obtained high-quality nano-DESI/HR-MS spectra of both laboratory-generated and field-collected aerosol samples while consuming only a small amount (<10 ng) of material [69]. Furthermore, it has been demonstrated that because of the short residence time of analyte molecules in the solvent (seconds), DESI and nano-DESI preserve [34,69] chemically labile aerosol constituents that cannot be detected using more traditional ESI/HR-MS analysis that expose the analyte molecules to the solvent for significantly longer periods of time (minutes).

The unique utility of DESI and nano-DESI/HR-MS approaches for understanding molecular transformations of OA resulting from atmospheric ageing processes has been demonstrated in a number of studies employing targeted laboratory experiments [34,64–66,69] and analysis of samples collected in field campaigns [67,68]. For example, recent laboratory studies have demonstrated that biogenic SOA produced by oxidation of d-limonene (limonene SOA) can be transformed from predominantly scattering 'white' aerosol into light-absorbing 'brown' aerosol as a result of gas–particle reactions between its carbonyl constituents and ammonia [34,69,71,72]. Figure 2 provides an illustration of this atmospheric 'browning' chemistry,

wherein limonene SOA collected on Teflon substrates turns from white to brown after several hours of exposure to parts per billion (ppb) levels of gaseous ammonia in the presence of water vapour. DESI and nano-DESI analyses indicated the chromophores responsible for the observed browning of limonene SOA were likely highly conjugated N-containing organic compounds (NOC) [34,69]. These chemically labile NOC could not be detected using traditional ESI analysis of limonene SOA solvent extracts [71].

In a follow-up study, Nguyen *et al.* used nano-DESI/HR-MS to probe effects of dissolution, evaporation and redissolution of limonene SOA in the presence and absence of ammonium sulphate on the chemical composition of SOA [65]. It has been demonstrated that water evaporation from droplets containing common atmospheric mixtures of SOA/ammonium sulphate can greatly accelerate reaction processes, leading to the formation of NOC, of which some exhibit strong light-absorbing properties. Quantitative estimates performed in that study indicated the molar fraction of the NOC chromophores was less than 2%, while their overall effect on the effective mass absorption coefficient in the visible wavelength range was dominant, resulting in the effective absorption mass coefficient for the aged limonene SOA material in excess of 10^3 cm^2 g^{-1}. These results suggest that trace amounts of chromophoric compounds may define the SOA material's overall optical properties [65]. These laboratory observations were later corroborated by the results obtained for field-collected samples of SOA, where higher fractions of NOC were identified in the night samples [67,68]. Consistent with the laboratory experiments, higher relative humidity (RH) and lower nighttime temperatures facilitate aqueous-phase reactions of amines/ammonia with aldehyde/carbonyl species in deliquesced particles [34]. An additional study using the nano-DESI/HR-MS approach compared the chemical composition of OA formed in laboratory-controlled chamber experiments and field samples collected at rural and urban sites during the CalNex 2010 field campaign [68]. The results of this comparative study indicated the composition of ambient SOA from an urban environment exhibited substantial overlap with the chamber experiments, where model aerosol was prepared from photooxidation of diesel fuel fumes, suggesting a promising approach for future studies to improve the fundamental understanding of SOA chemistry and sources.

Another example of fundamental reaction chemistry revealed by the nano-DESI/HR-MS approach was demonstrated in a laboratory study investigating the effects of RH on the composition and concentrations of SOA generated by photooxidation of isoprene [66]. Figure 3 shows mass spectra of SOA formed under dry (2% RH) and humid conditions (90% RH). Clearly, SOA formed at high RH contains a significantly smaller number of high-MW oligomers compared to the dry conditions. This result was attributed to the shift in chemical equilibria of the particle-phase condensation/oligomerisation reactions, such as esterification, toward the reactants. An important implication of these chemical differences could be lower water solubility and higher viscosity of SOA produced under dry conditions. These properties may have an effect on the physical state of OA [66], leading to potential formation of semi-solid or glassy states of particles [73–75] with subsequent consequences on the kinetics and chemistry of their atmospheric oxidation, hygroscopicity, ability to nucleate cloud droplets and ice crystals and overall lifetime of SOA particles in the atmosphere.

If corresponding chemical standards are available and their ionisation efficiency is not too sensitive to matrix effects, both DESI and nano-DESI can be employed for quantitative analysis of selected organic molecules present in aerosol mixtures using calibration measurements. For instance, successful quantitative detection of selected polycyclic aromatic hydrocarbons (PAHs) [62] and dicarboxylic acids [63] has been reported for field-collected samples of

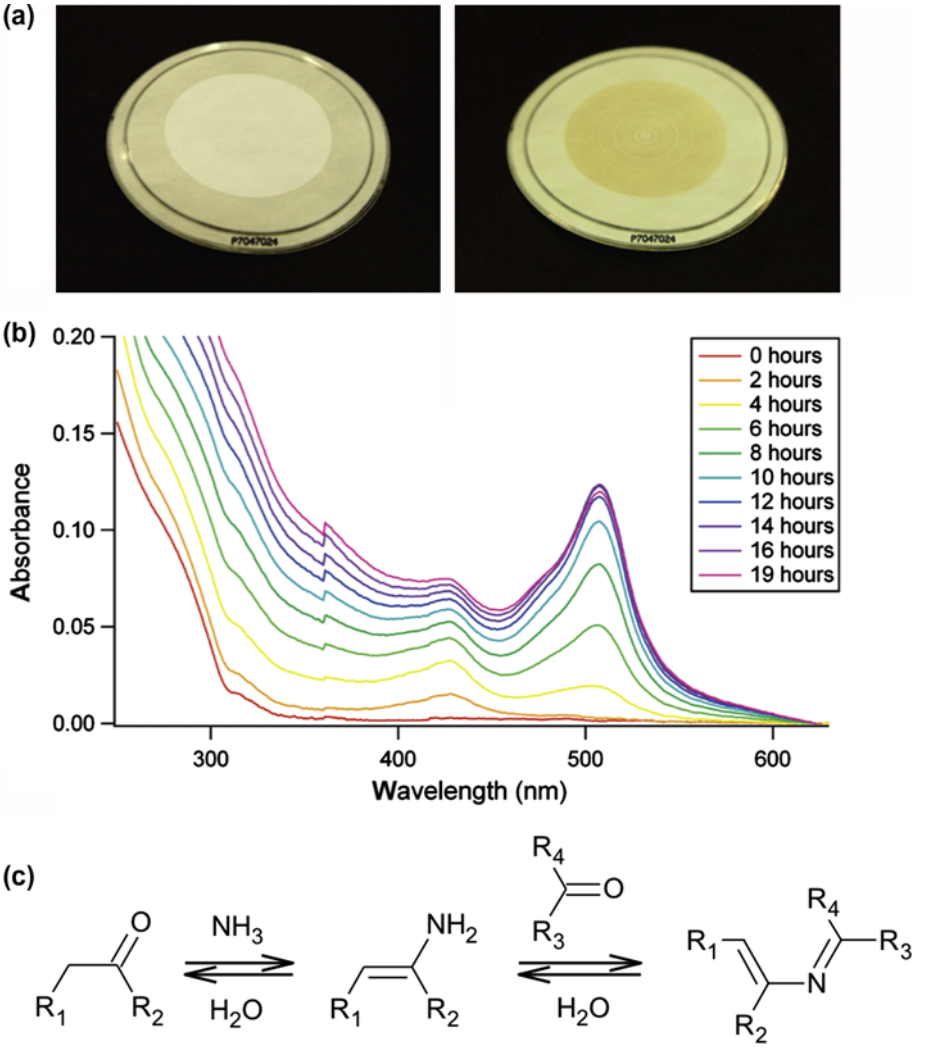

Figure 2. (Colour online) (a) Photographs of a limonene SOA sample generated by ozonolysis of d-limonene. Limonene SOA is initially white (left-hand side image) but changes color to brown (right-hand side image) after several hours of exposure to ppb levels of NH_3. (b) UV–visible spectra of limonene SOA collected during 'browning' reactions with NH_3(g). (c) A generalised reaction mechanism of carbonyl-to-amine conversion inferred from comparative analysis of 'white' and 'brown' samples using DESI/HR-MS. Reproduced with permission from Ref. [34].

biomass burning aerosols and verified by independent gas chromatography–MS measurements. The use of different solvents and their mixtures may be employed for targeted analysis of different classes of organic compounds based on their solvent-specific solubility [76]. In addition, doping solvent with a derivatising reagent at different concentrations enables *reactive* DESI and nano-DESI/HR-MS experiments, where selected analyte molecules may be

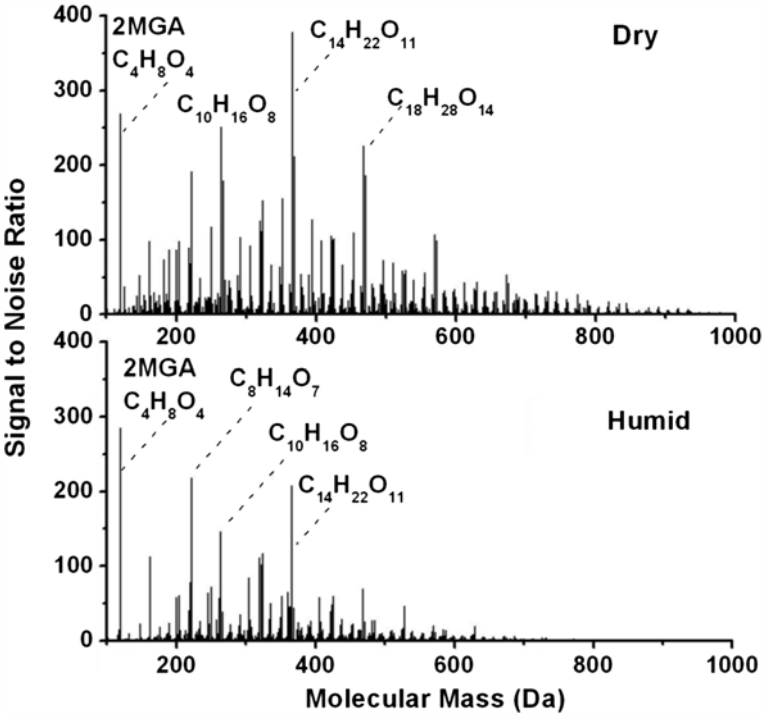

Figure 3. Stick spectra of all assigned compounds in SOA samples generated by photooxidation of isoprene under dry (2% RH) and humid (90% RH) conditions. To facilitate spectra comparison and eliminate differences occurring from different ionisation mechanisms, the horizontal axis corresponds to molecular weights of the neutral SOA compounds. High-MW oligomeric species in the dry sample are significantly more abundant. Reproduced with permission from Ref [66].

separated from the complex mixture based on their specific chemical reactivity with the reagent [70,77,78]. For example, the Girard's T (GT) reagent efficiently reacts with cholesterol, enabling sensitive detection of this low ionisation efficiency compound [78]. Furthermore, these experiments may be used to estimate concentrations of a large subset of individual analyte molecules that cannot be quantified using any existing analytical approaches [70].

Figure 4(a) illustrates the reactive nano-DESI/HR-MS experiment performed for quantitative analysis of selected individual limonene SOA constituents using the GT reagent [70]. The GT reagent [79] is an quaternary ammonium salt with the structural formula $[(CH_3)_3N^+CH_2C(=O)NHNH_2]Cl^-$. Once dissolved, the hydrazine group in the corresponding cation (GT^+) reacts selectively with molecules (M) containing carbonyl groups, such as aldehydes and ketones [79], forming either direct adducts $[M+GT]^+$ or their dehydrated co-products $[M–H_2O+GT]^+$ [80]. Characteristic shifts in exact masses of peaks observed before and after doping the solvent with GT identify the reactant–product pairs produced during reactive nano-DESI experiments as indicated by black (reactants) and red (products) colors in the figure. An important feature of these reactions is that positively charged GT^+ tag converts neutral carbonyl compounds into charged adducts, thereby enabling uniform ionisation and

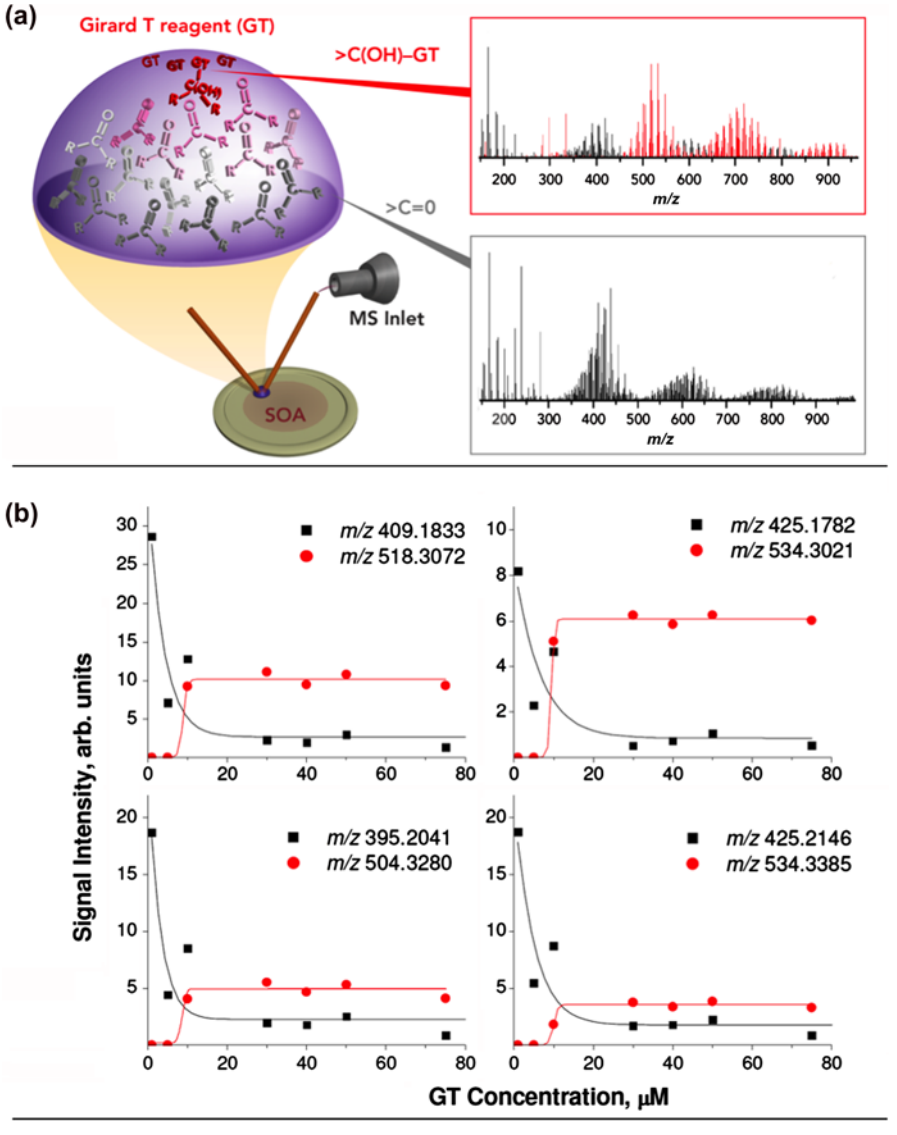

Figure 4. (Colour online) (a) Schematics of the reactive nano-DESI/HR-MS experiment and the corresponding spectra of limonene SOA material probed with pure acetonitrile (top) and with 50 μM of GT in acetonitrile (bottom). Peaks corresponding to the products of reaction between limonene SOA and GT are highlighted in red. Unreacted constituents of limonene SOA are shown in black. (b) The dependence of signal intensities of selected peaks corresponding to limonene SOA-reactive constituents (black squares) and their $[M+GT]^+$ products (red circles) on the GT concentration. Reproduced with permission from Ref. [70].

minimising discrimination against low proton affinity species. The concentrations of individual molecules undergoing reaction with GT^+ can be estimated by monitoring the yield of the GT adduct as a function of GT concentration in the solvent and assuming uniform ionisation

efficiency of the GT^+ and the $[M+GT]^+$ ions [70]. Figure 4(b) shows the yields of selected $[M+GT]^+$ products and the decay of the corresponding reactants as a function of GT concentration in the solvent. The signals of the $[M+GT]^+$ products reach saturation at the GT concentration of ~10 μM. Above this concentration, GT^+ is supplied in excess. Therefore, the saturated intensities of the $[M+GT]^+$ products are proportional to the corresponding concentrations of the analyte molecules, M. Concentration of the individual molecule, M, is estimated by dividing the $[M+GT]^+$ signal intensity in the plateau region by the ionisation efficiency of GT^+ derived from the same experimental data. Using this approach, an amount of ~0.5 pg of the most abundant limonene SOA dimer and the total amount of dimers and trimers at the level of ~11 pg were estimated in the area of ~1 mm^2 sampled by the nano-DESI probe [70]. Although the reported study used GT reagent, this approach can be readily extended to other charged reagents [49].

Cooks and co-workers also used reactive DESI to study reactions of organic molecules trapped in charged microdroplets and isolated solvent-free organic cations with molecules on surfaces [81–83]. Girod *et al.* [81] demonstrated rate enhancements by several orders of magnitude for model bimolecular reactions occurring in microdroplets compared to bulk solution. In these experiments, the pneumatically assisted spray of charged droplets containing GT was directed at an area along the surface normal for 5 min. The resulting material subsequently was washed and analysed using nanoelectrospray ionisation (nanoESI). The results indicated efficient reaction between GT and analyte molecules present on the surface. Spatial analysis of the surface indicated the reaction occurs in secondary droplets that are later deposited onto the surface, forming a ring around the area interrogated by DESI. Time-resolved experiments demonstrated the reaction in a liquid film on the surface is insignificant. The lack of reaction products in the nanoESI spectrum of a solution containing both reactants indicated that the size of the microdroplet has a significant effect on the reaction rate. The authors suggested that as the droplet size decreases, the pH of the solution decreases. Meanwhile, the concentrations of the reagents increase, driving the reaction to completion. The observed differences between nanoESI and reactive DESI results were attributed to a smaller size of secondary droplets (0.8–1.9 μm) generated in DESI experiments. Adding water to the spray solution results in larger droplets and lower product yields. Similar rate enhancement was observed when one of the reactants present in the vapour phase was captured in microdroplets containing the second reactant [82]. Furthermore, Badu-Tawiah *et al.* demonstrated efficient reaction between bare organic cations and ambient surfaces [83]. In that study, fully desolvated ambient 2,4,6-triphenylpyrylium cations produced using ESI were allowed to react with a dry film of ethanolamine on a solid surface. The results demonstrated that only one product was generated under these reaction conditions, while the solution-phase reaction resulted in formation of two distinct isomeric products.

Chemical characterisation of substrate-deposited OA samples also has been performed using an ASAP-MS, which employs a different approach for analyte pickup and ionisation [36]. In this technique, a heated stream of nitrogen gas evaporates analyte molecules from the substrate. Evaporation is followed by proton transfer ionisation in the presence of H_3O^+ to produce $[M+H]^+$ ions [84]. Interestingly, non-polar molecules are ionised in ASAP as molecular radical cations, which may be advantageous for structural characterisation of complex analytes [85]. An important advantage of ASAP-MS is that poorly soluble compounds can be probed without using solvents. Moreover, the evaporation rate of the analyte can be experimentally controlled by varying the temperature of nitrogen gas, allowing quantitative

measurements of the vapour pressure of low-volatility organic compounds. These data are critically important for predicting particle formation and ageing in atmospheric models. Figure 5 shows the results obtained in a temperature-programmed ASAP-MS experiment reported recently by Bruns *et al.* [86]. In that study, the technique's performance was demonstrated using pyrene, a chemical standard with well-known vapour pressure, as a model system. Figure 5(a) shows the experimentally measured evaporation rate (E_t) as a function of time and temperature. The value of E_t, in mol s^{-1}, is calculated using Equation (1):

$$E_t = N_0 \times \frac{I_t}{I_{\text{total}}} \tag{1}$$

where N_0 is the number of molecules in the probed sample calculated from the known mass loading. I_t is a signal intensity of the pyrene peak at time t, while I_{total} is its integrated value over the entire duration of the experiment. The vapour pressure was derived from the averaged

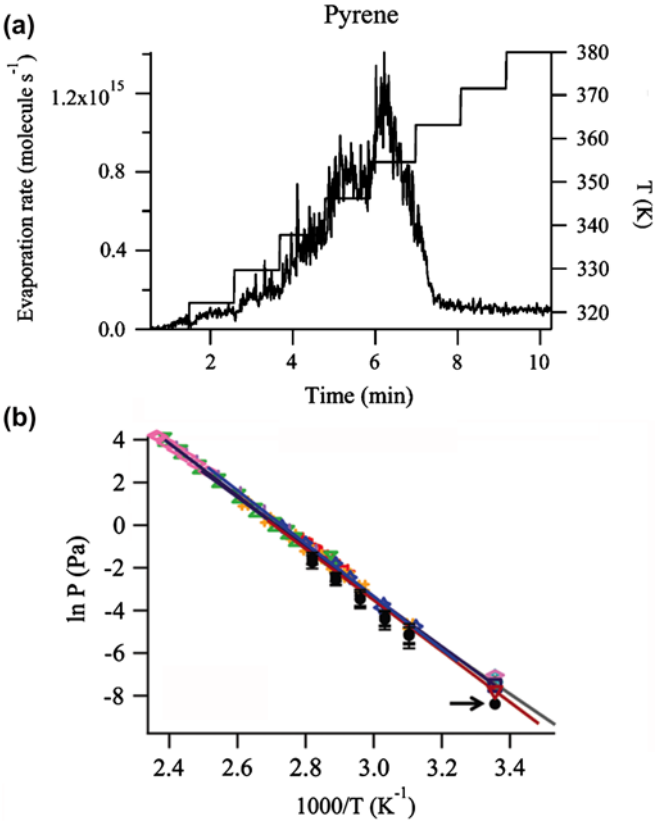

Figure 5. (Colour online) (a) Evaporation rate as a function of time and temperature for pyrene measured in a temperature-programmed experiment using ASAP-MS detection. (b) Natural log of pyrene vapour pressure as a function of inverse temperature determined from the ASAP-MS measurements (black dots) in comparison with previously published data (coloured symbols). Reproduced with permission from Ref. [36].

(E_T) values corresponding to isothermal time periods at different temperatures (T) using the Langmuir's model of evaporation (Equation (2)):

$$P_T = E_T \frac{\sqrt{2\pi \mathrm{RTM}}}{N_\mathrm{A} S_T} \tag{2}$$

In this equation, R is the gas constant, M is the molar mass, N_A is the Avogadro number and S_T is the surface area of the sample that was estimated based on visual observations and assuming a flattened sphere geometry. The heat of sublimation (ΔH_sub) was determined from the slope of the Clausius–Clapeyron plot (Figure 5(b)), as shown in Equation (3):

$$\ln P_T = -\frac{\Delta H_\mathrm{sub}}{RT} + \mathrm{Const} \tag{3}$$

Similar experiments were performed for a number of dicarboxylic acids. Although the heats of sublimation obtained from ASAP-MS experiments were in excellent agreement with the literature values, vapour pressures were lower than the values obtained using other techniques by a factor of 2 and 3. The authors attributed this discrepancy to the relatively slow diffusion of molecules during sample evaporation at atmospheric pressure (AP) compared to effusion in vacuum-based techniques. Nevertheless, results of the initial ASAP-MS measurements were quite promising. For example, ASAP-MS measurements correctly reproduced the even/odd alterations in the vapour pressure of dicarboxylic acids as a function of the number of carbon atoms reported in a separate study of Cappa *et al.* [87]. Other solvent-free ambient ionisation techniques, including laserspray ionisation and its analogues [88,89] can be used for the analysis of non-polar and poorly soluble analytes in complex organic samples.

EESI-MS [90] is another promising ambient ionisation method for online analysis of aerosols. In EESI-MS of aerosols, a mist of charged droplets produced by electrospray is crossed with a flow of air containing particles in front of an MS inlet. The first application of EESI-MS to α-pinene + O_3 SOA by Doezema *et al.* [37] showed that both the particle and gas-phase components of aerosols can be detected with protonation serving as the primary ionisation mechanism. They reported a significant enhancement of oligomeric compounds in SOA prepared at 50% RH in the reaction chamber compared to the SOA generated in dry air. This contrasts previous observations [66,91] in isoprene high-NO_x, where the oligomeric content was reduced in humid air. Further examination of the effects of RH on SOA molecular composition is clearly warranted.

The field of ambient surface ionisation techniques is undergoing rapid growth both in method developments and applications. Thus far, few of the techniques described earlier have been used for chemical characterisation of aerosol samples. The following discussion highlights several recent developments in ambient surface ionisation techniques that have the potential for analyzing aerosol samples. For example, Nudnova *et al.* [92] described an ambient ionisation approach, wherein neutral compounds evaporating from an organic film, either spontaneously or as a result of laser desorption, are ionised by plasma sustained inside a MS capillary inlet. The method is suitable for analysis of particle filter samples and potentially can be used in a surface imaging mode with spatial resolution characteristic of laser desorption methods. Ho *et al.* [93] presented a paper-based surface acoustic wave (SAW) sample delivery and ionisation source, where a solvent phase organic analyte absorbed by the

paper is atomised by SAW activated using the underlying piezoelectric element. Surface electric field induced by SAW results in polarisation of the liquid film at the substrate and subsequent charging of the atomised droplets from which gas phase ions are produced upon evaporation. Organic standards or heavy metals at concentrations as low as 1 nM were successfully detected using both positive and negative ion modes, suggesting the great potential of this method for aerosol analysis and environmental monitoring.

Guenther *et al.* [94] used a method related to EESI to post-ionise electrosurgical aerosol produced by rapid heating of biological tissues. The electrosurgical aerosol contains a detectable amount of ions, which are dominated by fragments of phospholipids. In EESI, the ion current in the positive ion mode increased by a factor of 20–50 and produced largely intact phospholipid ions extracted from the neutral particles by the electrospray. No ion current enhancement was observed in the negative ion mode. In a variation of the EESI-MS method, the ionising spray was charged by a corona discharge [95]. The advantage of the corona discharge is in its ability to ionise analytes that do not typically appear in ESI mass spectra. For example, Hu *et al.* was able to detect radical cations of non-polar compounds, such as benzene and cyclohexane, while polar compounds, such as acetone, acetonitrile and oxygenated terpenes, appeared as protonated species in the spectrum. The method tolerates complex matrices, making it suitable for analysis of environmental samples, including extracts from aerosols.

2.2. *Secondary ion mass spectrometry*

In contrast with the ambient ionisation techniques, surface analysis using secondary ion mass spectrometry (SIMS) is performed in vacuum. SIMS involves sputtering molecules from surfaces using energetic bombardment with a primary ion beam followed by the analysis of secondary ions using MS [96,97]. Although a variety of mass analysers can be used for the detection of secondary ions, time-of-flight (TOF) instruments are particularly attractive because they enable fast acquisition of mass spectra over a broad range of mass-to-charge ratios (*m/z*) [98,99]. This capability is critical for detailed characterisation of the spatial distribution of both organic and inorganic species in complex samples with good sensitivity and in a reasonable amount of time.

TOF-SIMS has been extensively used for chemical characterisation of both field-collected and laboratory-generated particles [100–106]. For example, Figure 6 shows TOF-SIMS maps obtained for particles of marine origin collected in a field study at Point Reyes National Seashore (Marin County, CA) [104]. The ion maps indicate that methanesulfonate ($CH_3SO_3^-$) and sodium (Na^+) are present in the same type of particles, while bisulphate (HSO_4^-) is a characteristic marker of another type of particles. On the basis of additional chemical imaging information presented in that study, two externally mixed classes of sulphur-containing particles corresponding to chemically modified (atmospherically aged) sea salt particles and sulphate particles formed by gas-phase oxidation of sulphur-containing compounds were identified. Combined particle characterisation using TOF-SIMS and microspectroscopy techniques employed in that study afforded the first quantitative speciation of S(VI) and S(IV) forms of sulphur in individual particles. These data are indicative of the formation mechanisms and atmospheric ageing history of marine particles, which is of particular importance for modelling atmospheric chemistry and physics in marine boundary layers [107].

Tervahattu *et al.* used dynamic TOF-SIMS for molecular speciation of organic coatings observed on ambient particles representative for marine [100] and continental [103] areas.

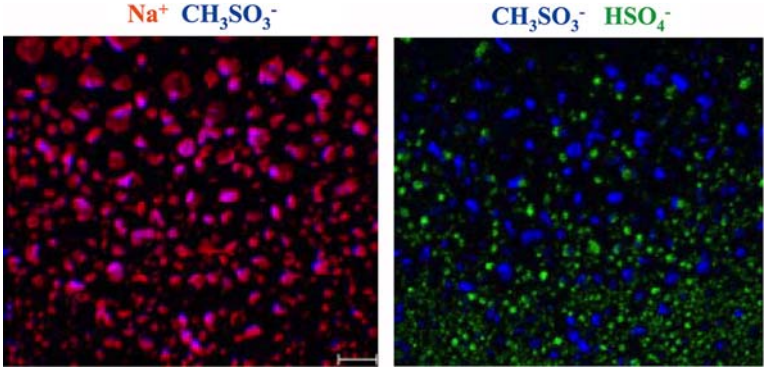

Figure 6. (Colour online) TOF-SIMS maps of typical samples collected at the ground site located in Point Reyes National Seashore: (a) Overlaid maps of the Na^+ and $CH_3SO_3^-$ ions. Their close overlap indicates formation of methanesulfonate in sea salt particles. (b) Overlaid maps of $CH_3SO_3^-$ and HSO_4^- ions indicate external mixing of sea salt and ammonium sulphate particles. Maps are 100 μm × 100 μm. Reproduced with permission from Ref. [104].

Their results showed the presence of palmitic and other fatty acids in the particles' outermost layers, corroborating predictions from earlier modelling and laboratory studies that suggested common existence of the fatty acid surfactants on atmospheric particles [108,109]. These studies indicated the need for a better understanding of the chemical reactivity, physical and optical properties of surfactant-coated particles and their impact on the atmospheric environment.

The examples discussed earlier demonstrate the potential of TOF-SIMS for characterising the internal composition and surface chemistry of aerosol particles. However, the lateral resolution of the commercial instruments is insufficient for detailed mapping of the chemical composition of individual particles. To address this problem, Sakamoto *et al.* developed a new high spatial resolution TOF-SIMS instrument [110]. In this apparatus, SIMS is coupled with scanning electron microscopy that enables easy localisation of particles for TOF-SIMS imaging. In addition, focused ion beam may be used for sectioning particles prior to analysis. This approach is important for studying the internal structure of inhomogeneous particles. The instrument's performance was demonstrated for two 1.7 and 5.4 μm diameter field-collected aerosol particles.

Two other studies focused on the development of new approaches for improved sensitivity and mass resolution in SIMS. Specifically, Fletcher *et al.* developed a new dynamic TOF-SIMS instrument that uses a continuous primary ion beam (C_{60}^+, 40 keV) [111]. In this instrument, secondary ions undergo collisional cooling in a radio frequency (RF)-only quadrupole. The ions are subsequently transferred to a linear buncher that generates short pulses of ions for analysis in the TOF section. This process efficiently decouples secondary ion formation from mass analysis, enabling independent optimisation of mass resolution and significantly increasing the duty cycle, hence the instrument's sensitivity. Furthermore, it supports tandem mass spectrometry, or MS/MS, experiments critical for structural characterisation of complex molecules. In a related study, Carado *et al.* reported on the implementation of SIMS on a commercial hybrid-quadrupole orthogonal TOF-MS [112]. This instrument also

uses a continuous ion beam, which significantly increases the duty cycle, and the sensitivity. The ions undergo collisional cooling and focusing in a quadrupole ion guide and are analysed using a high-resolution orthogonal TOF-MS. Mass resolving power of ~15,000 with an *m/z* range up to 40,000 demonstrated with this instrument enables simultaneous chemical analysis of small and large molecules. These capabilities will be very useful for unraveling the complexity of individual atmospheric particles collected on substrates.

Because TOF-SIMS of atmospheric particles generates fairly complex mass spectra, the development of new data analysis tools is critical to extracting maximum information from the experimental data. Principal component analysis is commonly used to classify complex TOF-SIMS spectra. Recently, Kalegowda and Harmer examined the performance of several statistical analysis tools for classification of TOF-SIMS spectra of complex copper-iron sulphide mineral samples [113]. Two methods, soft independent modelling of class analogy and k-nearest neighbour classification, were identified as the most accurate techniques for particle classification. In addition, these methods enabled the classification of particles containing the same elements but different crystal structures. These results are particularly remarkable because of the complexity and similarity between the experimental spectra obtained for different particle types.

Cameca's recent development of NanoSIMS instruments has opened up new opportunities for accurate measurements of the elemental composition and isotope ratios. NanoSIMS is a microprobe instrument that combines the sensitivity of dynamic SIMS with relatively high mass resolution necessary for separation and unambiguous identification of isotopic peaks (e.g. $^{13}C^{14}N^-$ vs. $^{12}C^{15}N^-$ at *m/z* 27.016 and 27.009, respectively). The combination of high spatial resolution (down to 50 nm), high sensitivity (parts per million, ppm, in elemental imaging) and high mass resolution has made this instrument one of the most sensitive tools for spatially resolved elemental and isotopic analysis of complex surfaces. Although most applications of NanoSIMS are related to imaging of biological materials [114–119] and soil aggregates, several groups explored the potential of this technique for chemical characterisation of ambient particles. For example, McIntire *et al.* demonstrated the utility of NanoSIMS in studying the three-dimensional (3D) structure of complex organic particles [120]. The observed increase in the oxygen-to-carbon ratio toward the interior of organic particles produced during ozonolysis of surface bond alkenes indicated the polar groups are buried inside the particle's hydrophobic shell.

Winteholler *et al.* used NanoSIMS' high sensitivity for measuring sulphur isotope ratios of individual particles down to 500 nm in diameter [121]. In that study, sulphur isotope ratios were measured for several atmospherically relevant minerals. Particle-to-particle reproducibility of 2–5% was reported for submicron particles with the lowest precision observed for particles with complex topographies. The $^{34}S/^{32}S$ ratio varied by ~15% between different mineral samples, indicating measurable matrix effects on the observed isotope ratios. A fundamental understanding of the effect of particle morphology and composition on isotope ratio measurement accuracy is necessary for improved performance of NanoSIMS for individual particle characterisation.

Recently, Harris *et al.* examined that sulphur isotope undergoes fractionation during oxidation of SO_2 in the gas phase, liquid phase and on mineral dust particle surfaces using NanoSIMS of collected products [122,123]. Oxidation of sulphur dioxide to sulphate is an important reaction in atmospheric chemistry [124]. The isotopic fractionation [125] (variation in the equilibrium distribution of the stable isotopes) typically results from slight differences

in bond strengths, velocities and diffusivities of molecules containing lighter vs. heavier isotopes. For example, the slightly higher evaporation rate of $H_2{}^{16}O$ compared to $H_2{}^{18}O$ from groundwater contributes to ^{16}O enrichment of atmospheric water vapour and cloud droplets. The fractionation constant is defined as the ratio of the heavy to light isotopes in the products divided by the ratio of the heavy to light isotopes in the reactants. For the sulphur isotope fractionation, the fractionation constant is given by Equation (4):

$$\alpha = \frac{(^{34}S/^{32}S)_{products}}{(^{34}S/^{32}S)_{reactants}} \quad (4)$$

When the heavy isotope reacts faster than the light isotope, the fractionation constant is greater than one ($\alpha > 1$). The fractionation factor of 1.008 at 19 °C was obtained for the gas-phase oxidation of SO_2 [123]. For aqueous oxidation, the fractionation factors of 1.0151, 1.0174 and 1.0118 were obtained when H_2O_2, O_3 and the H_2O_2/O_3 mixtures were used as oxidants, respectively [123]. The radical chain reaction catalysed by iron was the only reaction with a faster rate for the lighter isotope ($\alpha = 0.9894$ at 19 °C). It follows that isotope ratio measurements may be useful for distinguishing metal-catalysed oxidation of SO_2 from other competing pathways. Another study by Harris *et al.* demonstrated that sulphur isotope fractionation can be used for understanding the kinetics and mechanisms of SO_2 oxidation by mineral dust [122]. Sulphur isotope fractionation during heterogeneous oxidation of SO_2 on Sahara dust particles was characterised by a substantially larger fractionation factor ($\alpha = 1.0096$) than aqueous oxidation in Sahara dust leachate ($\alpha = 0.9917$). The authors proposed that a radical chain reaction pathway initiated by transition metal ions leached from the dust is the main mechanism of aqueous SO_2 oxidation in Sahara dust leachate [122]. In contrast, heterogeneous oxidation on dust particles primarily is controlled by particle composition. Very different fractionation factors were reported for ilmenite/rutile ($\alpha = 1.012$), feldspar ($\alpha = 0.948$) and clay ($\alpha = 1.085$). These results indicate that the isotope ratio measurements provide important constraints on the possible oxidation pathways of sulphur dioxide in the environment and contribute to a fundamental understanding of the homogeneous and heterogeneous oxidation of SO_2.

2.3. *Secondary neutral mass spectrometry*

Secondary neutral mass spectrometry (SNMS) relies on postionisation of the neutral molecules sputtered during surface bombardment by the primary ion beam. Postionisation results in significant signal enhancement and enables detection of a broader range of sputtered molecules. When combined with soft ionisation, SNMS is particularly well suited for imaging organic molecules in aerosol samples. Soft ionisation of sputtered organic molecules is performed using single-photon absorption of vacuum ultraviolet (VUV) light from a laser [126] or a tunable synchrotron radiation light source [23]. Tyler *et al.* [126,127] used 157 nm (7.9 eV) and 193 nm (6.4 eV) lasers for postionisation and imaging PAHs in individual field-collected aerosol particles. The samples were cryocooled to reduce the loss of semi-volatile PAHs in vacuum. Significant signal enhancement was observed for all PAHs examined in that study. Postionisation using a 193 nm laser resulted in 2–50-fold increases in the ion yield, while 157 nm postionisation resulted in a 1000-fold increase in the signal. Pyrene and

anthracene were efficiently ionised using both lasers. However, because of multiphoton ionisation processes, higher fragmentation yield was obtained using the 193 nm laser. In contrast, postionisation of naphthalene resulted in the formation of abundant fragment ions. In addition, an abundant $[M-H]^+$ peak was observed when sputtered naphthalene was ionised using the 157 nm laser. The authors hypothesised that because the ionisation energy (IE) of naphthalene (8.14 eV) is greater than the energy of both lasers, postionisation of a neutral $[M-H]^{\bullet}$ radical formed in the sputtering process is responsible for the formation of the $[M-H]^+$ ion. Figure 7 shows SNMS maps of naphthalene, anthracene and pyrene in ambient aerosol particles. The images were analysed using maximum autocorrelation factors (MAFs). This statistical analysis technique identified three particle types as shown in the regions of interest (ROIs) panel. The combination of laser-SNMS imaging with statistical analysis tools is ideally suited for studying surface chemistry of PAHs on ambient particle surfaces.

Imaging of smaller particles may become possible using recent instrument development efforts reported by Ebata *et al.* [128]. Their study described the development of a new laser ionisation mass nanoscope, in which the primary 20 keV Ga^+ ion beam can be focused to a diameter of 40 nm. Sputtered neutral molecules were ionised using a femtosecond laser. The ions subsequently were analysed using a high-resolution multi-pass TOF with a mass resolving power up to 40,000. In comparison with SIMS, postionisation of neutrals resulted in a 1000-fold increase in the signal of silver ions.

Takahashi *et al.* demonstrated the utility of wavelength-tunable postionisation of sputtered neutrals for chemically selective SNMS imaging [129]. Quasi-continuous tunable radiation from a synchrotron light source enabled acquisition of SNMS spectra at 10 kHz repetition rate. Furthermore, the wavelength of the radiation may be tuned to affect selective ionisation

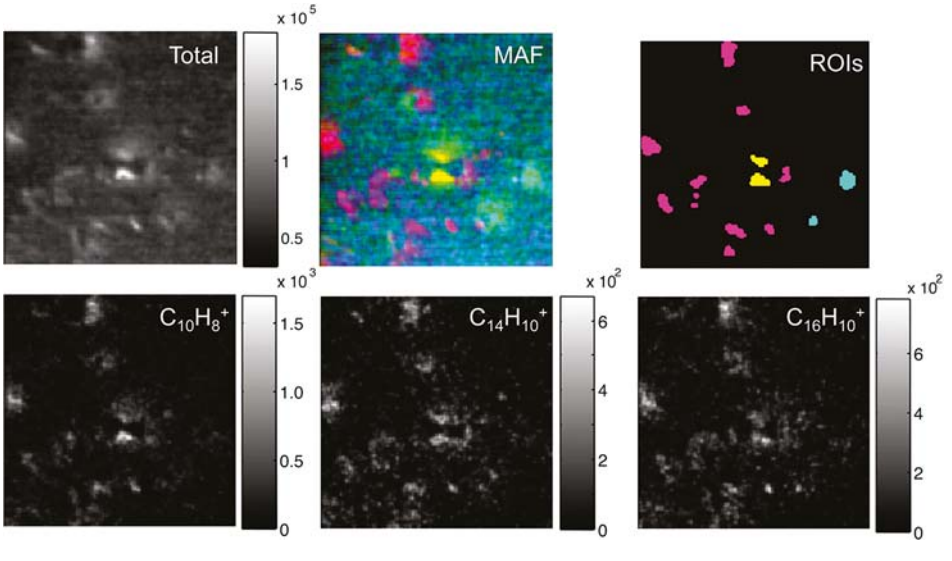

Figure 7. (Colour online) $75 \times 75\ \mu m^2$, laser-SNMS (157 nm) images of ambient aerosol particles from impactor stage 6 (2–3.5 μm in aerodynamic diameter). The top row shows the total ion image, a red–green–blue overlay of MAF factors 1–3 and ROI corresponding to the three particle types identified in the analysis. The lower row shows the molecular ion images for naphthalene, anthracene and pyrene. Reproduced with permission from Ref. [126].

of low-ionisation efficiency (IE) compounds, such as PAHs, or for efficient ionisation of all organic compounds, including high ionisation energy aliphatic organic molecules. Finally, it has been demonstrated that photoionisation efficiency (PIE) curves can be acquired by scanning the wavelength of the light. PIE curves provide important structural information for both organic and inorganic molecules. VUV-SNMS of monolignols [130] produced spectra dominated by the molecular ions. The PIE curves of fragment ions were shifted towards lower energies, indicating significant vibrational excitation of the sputtered neutral molecules. The photofragment yield can be reduced by increasing the extraction delay time. This observation was rationalised assuming that molecules with lower internal energies also have lower kinetics energies.

2.4. *Laser desorption ionisation mass spectrometry*

A similar approach has been used for the online characterisation of airborne particles produced in smog chamber experiments. These experiments typically use single-photon VUV ionisation of neutral molecules formed during thermal desorption of particles [23,131,132]. Tunable VUV photoionisation reduces fragmentation of SOA constituents prior to analysis, which greatly simplifies the observed mass spectra. Using this technique, Fang *et al.* conducted detailed characterisation of the composition of SOA produced through photooxidation of several VOCs in a smog chamber [133,134]. It has been demonstrated that accurate measurement of the ionisation energies of individual SOA constituents provides important structural information that is difficult to obtain using other techniques. Specifically, PIE measurements enable differentiation between different isomeric species [23]. Gloaguen *et al.* examined the kinetics of ozone reaction with sodium chloride particles coated with anthracene [135]. Ozonolysis produced oxygenated anthracene molecules with up to five oxygen atoms. The ionisation energies of all the products has been determined from the corresponding PIE curves. However, the lack of data on the IE of oxygenated anthracene molecules made it difficult to assign structures to the observed products.

Bertram and co-workers developed a broadly tunable, laboratory-based VUV light source and demonstrated its applications for characterisation of single particles down to 300 nm in diameter when coupled to an ion trap mass spectrometer [136]. In a follow-up study from the same group [137], this instrument was used to characterise single-component particles of oleic acid and dihydroxybenzoic acid (DHB). In that study, particle vaporisation was performed using a CO_2 laser. The degree of fragmentation observed in mass spectra was a strong function of vaporisation energy and the analyte molecule's properties. For example, at low vaporisation energies, DHB was observed as intact ions, while significant fragmentation was observed for oleic acid. The observed fragmentation was attributed to the unimolecular dissociation of vibrationally excited molecules following the ionisation step. Simpson *et al.* examined the effect of particle composition on the observed fragmentation in VUV mass spectra of two-component oleic acid-oleyl alcohol particles [138]. They found the degree of fragmentation of individual components in mixed particles depends on the particle composition. Specifically, the addition of oleyl alcohol resulted in enhanced fragmentation of oleic acid. This observation was rationalised assuming that the presence of oleyl alcohol results in more efficient heating of oleic acid during the laser vaporisation process. Furthermore, the degree of fragmentation did not show a linear dependence on the

molar ratio of oleic acid in the particle, indicating that quantification using this approach is challenging.

Geddes *et al.* [139] described a near-infrared (IR) laser desorption ionisation method with sufficient sensitivity to produce mass spectra of OA at realistic atmospheric mass concentrations ($\sim$1 $\mu g/m^3$) and with good time resolution (2 min). The aerosols first are collected on an aluminum probe then desorbed/ionised with a 1064-nm laser pulse. Little or no fragmentation was observed in mass spectra of model aerosols of oleic acid and SOA produced through ozonolysis of α-pinene.

2.5. *Laser ablation mass spectrometry*

LA-MS has been extensively used for analysing surfaces and ambient particles [45,140,141]. The technique uses an intense laser beam for volatilisation and ionisation of material from a surface. LA is a highly non-linear process, in which the amounts of material removed from the surface, the plume's composition, and the heating of the material strongly depend on the irradiance (energy per unit time and area) [45,140]. In addition, the spatial profile of the laser beam, pulse duration and wavelength significantly influence the LA process [140]. Particles, molecules, atoms and ions are ejected from surfaces following laser irradiation [142]. Significant heating of the ablated material results in facile fragmentation of molecules and ions, making it difficult to determine molecular and structural information based on LA mass spectra [143]. However, LA is well suited for spatially resolved elemental analysis of surfaces. By far, coupling LA with inductively coupled plasma MS (LA-ICPMS) is the most popular approach for sensitive mapping of the elemental composition of surfaces without special sample pretreatment [45,144]. In LA-ICPMS, the laser-generated aerosol is transferred to the ICP source, where it is vaporised and ionised by the plasma. The high sensitivity and dynamic range of this technique enable simultaneous detection of both major and minor constituents of the sample. Although this technique has been used primarily in materials science applications, recent studies examined the utility of LA-ICPMS for analysis of soil and ambient particles [141,145–147].

The duration of the laser pulse plays an important role in LA-ICPMS experiments [44,148]. The use of nanosecond lasers is associated with several undesirable effects, including significant material redistribution, preferential evaporation of certain materials and absorption of the laser light by the plume, that further alters the plasma composition. In contrast, femtosecond ablation causes significantly less surface damage and dramatically suppresses the fractionation and matrix effects in LA-ICPMS [148]. It has been demonstrated that the crater shape, plume composition and size of ejected particles are critical factors that determine the utility of femtosecond LA for quantitative elemental mapping of materials. Further improvement in quantification using femtosecond LA-ICPMS requires better understanding of the dynamics of the plasma formation following laser irradiation. Koch *et al.* used shadowgraphy and light scattering to visualise shockwave propagation and particle ejection during femtosecond LA [149]. This study demonstrated the initial gas compression following laser irradiation is followed by a second shockwave caused by material ejection and air breakdown away from the surface. Multimodal particle size distributions observed in these experiments were attributed to different mechanisms of particle formation in the LA plume. Interestingly, submicron particles were produced during LA of Y:ZrO_2, while LA of $Li_2B_4O_7$ generated larger particles.

Several groups examined the performance of LA coupled with atomic force microscopy (AFM) or near-field optical microscopy for high-resolution chemical imaging of surfaces

[150–153]. It has been demonstrated that near-field LA can be used for reducing the size of the ablation area down to 100 nm in diameter. However, the sampling efficiency of ions formed in the process typically is fairly low. Zhu *et al.* combined AP near-field LA with sampling and postionisation of neutrals inside the vacuum system [150,153]. Such coupling enables chemical imaging of surfaces with spatial resolution of 5 μm [153]. That study reported the combined sampling efficiency of 10^{-4} [150]. Sampling efficiency is determined by the transfer efficiency of neutrals into the vacuum system (~0.1) and the IE (10^{-3}) obtained using electron impact ionisation. Although this technique has not been used to analyse small particles, the spatial resolution attainable using near-field LA is sufficient for such analysis.

3. Depth profiling

Several depth profiling MS techniques have been developed for applications in materials science and biology. A vast majority of these techniques rely on controlled removal of material from a solid or liquid surface using laser irradiation or ion beam bombardment [154]. Despite significant advancements in depth profiling instrumentation, detailed characterisation of submicron-sized particles still is a challenge. To the best of our knowledge, most studies have used SIMS for depth profiling of a collection of ambient aerosol particles [105,106,155,156]. In this section, we will discuss recent developments in depth profiling using MS that provide the basis to develop sensitive and robust approaches for detailed characterisation of the 3D structures of small particles.

Although SIMS is a fairly mature analytical technique, the formation of secondary ions during the energetic ion bombardment is a complex process that still is not well understood. It is well known that surface bombardment with monoatomic and small polyatomic primary ions results in significant surface damage [157–159]. Other important limitations of SIMS include substantial fragmentation of organic molecules [159,160] and relatively low ionisation yields [161]. Significant efforts have focused on addressing these limitations using beams of cluster ions [162,163]. It has been demonstrated that surface bombardment using keV C_{60}^+ ions significantly reduces surface damage and increases secondary ion yields [47]. Molecular dynamics simulations indicate that, in contrast with the monoatomic primary ions, the kinetic energy of the primary C_{60}^+ ions is deposited closer to the surface. As a result, C_{60}^+ bombardment results in a more efficient removal of material from a surface while generating a relatively shallow crater (~10 nm deep) [164]. This property of cluster beam bombardment is a key to accurate depth profiling using ion beams [154,162,163] and will be discussed later. Rabbani *et al.* compared the performance of C_{60}^+ and large, singly charged argon clusters for depth profiling using SIMS [165]. The results demonstrate that, in comparison with C_{60}, surface bombardment with large argon clusters results in gentler sputtering and reduces surface damage. However, secondary ion yields decrease with an increase in the argon cluster's size.

Chemical analysis of environmental particles on substrates using SIMS requires a fundamental understanding of the dependence of the sputtering yield on particle size. Molecular dynamics simulations indicate the sputtering yield for small gold nanoparticles (AuNP) and thin gold films are enhanced by up to a factor of three compared to the bulk gold [166]. The highest sputtering yields were predicted for 8 nm-gold particles and 3 nm-thick gold films. Yang *et al.* conducted an experimental investigation of size-dependent secondary ion yields during sputtering of AuNP in the size range of 10–100 nm by 20 keV C_{60}^{2+} primary ions [167]. Figure 8 compares the sputtering yield obtained for AuNP and a flat gold film. The

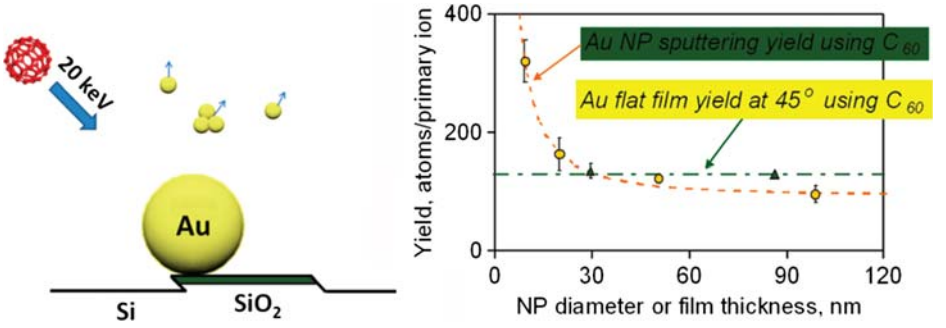

Figure 8. (Colour online) (a) A cartoon of the nanoparticle SIMS experiment and (b) sputtering yields for a planar gold film at 45° (triangles, dashed line) and nanoparticles (circles, dash-dotted line). Lines are shown as a guide. Reproduced with permission from Ref. [167].

results demonstrate that, indeed, the sputtering yield increases significantly with a decrease in the AuNP size. Specifically, the secondary ion yield obtained for 9.3 nm AuNP is ~3.3 times higher than for 98.8 nm AuNP. This study further demonstrated that without a good thermal contact with the support material, AuNP melt upon exposure to the primary ion beam but nevertheless largely retain their shape. AuNP melting was observed even when the sample stage was cooled to −107 °C. The authors suggested that good heat transfer between the particles and the substrate is necessary for quantitative SIMS depth profiling experiments.

Femtosecond LA-ICPMS has been used for depth profiling of thin metal coatings with 300 nm depth resolution and ~20 μm laser spot size [46]. Because the length of the laser pulse is short compared to thermal relaxation time, removal of material upon irradiation with a femtosecond laser is spatially confined and crater size is determined by the laser fluence and laser spot size. Figure 9 shows the dependence of the size and morphology of the craters generated using femtosecond LA. The crater formed after 15 laser shots has a rough bottom with an average depth of 1 nm and root mean square roughness of 10 nm. The observed roughness of the crater was attributed to the lateral inhomogeneity of the laser beam and the initial surface roughness. The amount of ablated material per pulse is on the order of 1 pg. It has been suggested that the sensitivity of ICPMS is sufficient for detecting material desorbed from a 100 nm diameter crater [46]. The volume of the crater increases linearly with the number of laser pulses. However, the proportionality constant depends on the properties of the ablated material. These findings highlight several important current limitations of LA depth profiling and provide important information for possible improvement of the lateral resolution and quantification using this technique.

Coupling LA with a softer ionisation using flowing atmospheric-pressure afterglow (LA-FAPA) enables formation of intact organic ions up to *m/z* 1000 [168]. Developed for ambient imaging of biological materials, this technique could be used in the future for imaging and depth profiling of ambient organic particles. The initial study by Shelley *et al.* [168] reported a spatial resolution of ~20 μm, depth resolution of ~40 μm and limit detection of five femtomoles for caffeine using LA-FAPA. In this experiment, LA was performed using a nanosecond laser, which is the major factor determining the depth resolution. Combining FAPA with a femtosecond laser may improve control of the LA process.

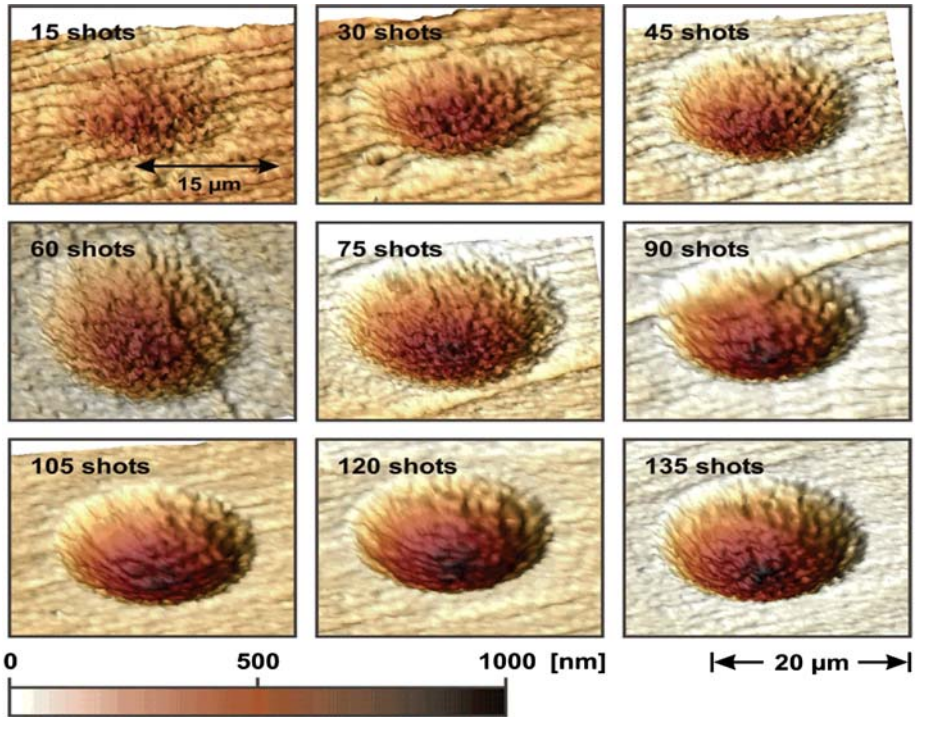

Figure 9. (Colour online) Three-dimensional pictures of the craters produced after different number of laser shots, measured using the AFM. Reproduced with permission from Ref. [46].

Valledor *et al.* performed depth profiling of thin metal films with nanometer depth resolution using pulsed-RF glow discharge TOF MS (RF-GD-TOFMS) [169]. In this technique, RF power generates plasma in argon, which sputters atoms and molecules from a surface. Sputtered species are subsequently analysed using a TOF mass spectrometer. Although the depth resolution of this technique is substantially higher than in LA-ICPMS, the lateral resolution is defined by the plasma size and typically is on the order of millimeters. Spatially resolved optical emission measurements identified two different RF-GD plasma regimes above a pure copper target [170]. The two plasma regimes resulted in similar sputtering rates but different plasma composition, demonstrating the complexity of the plasma-formation process. Further understanding of the physical phenomena underlying pulsed RF-GD sputtering is important for the development of this technique to facilitate accurate depth profile measurements.

A low-temperature plasma (LTP) probe combined with ICPMS enables depth profiling with lateral resolution of less than 10 µm and depth resolution of ~100 nm [171]. LTP-ICPMS is an attractive alternative to LA-ICPMS because it is easy to operate and may provide comparable performance. However, understanding the dependence of the crater's shape and the rate of material removal on experimental parameters still is rather limited, and phenomena associated with material sputtering require further characterisation.

Depth profiling of aerosol particles suspended in air has been performed using single-particle MS [172–174]. In these experiments, 'depth profiling' is performed by analyzing

a large number of identical particles exposed to different laser evaporation conditions. Woods *et al.* conducted a depth profiling study of glycerol particles coated with oleic acid [172]. In that study, gentle IR laser evaporation was followed by VUV ionisation of the vapour. At low laser fluences, only the particle's outer layers were evaporated in this process, while at higher laser fluences, the entire particle was evaporated, providing information on the chemical composition of the particle interior. For 2 μm particles, the technique was sensitive to changes in the oleic acid coating thickness of ~10 nm. Zelenyuk *et al.* reported depth profiling of NaCl particles coated with liquid dioctyl phthalate (DOP) layers and with solid pyrene [174]. Detailed size and shape measurements combined with depth profiling demonstrated that NaCl particles were completely coated with liquid DOP, while the pyrene coating was found to be non-uniform, forming aspherical particles with partially exposed NaCl cores. In another study, this group used depth profiling to examine the morphology of particles formed by mixing DOP with SOA of α-pinene [173]. The results of that study indicated phase separation of SOA and DOP in mixed particles. Furthermore, a thin layer of DOP was observed on top of SOA particles, indicating insoluble components may be present on particle surfaces and affecting their physicochemical properties.

4. Chemical analysis of airborne droplets

4.1. *Field-induced droplet ionisation mass spectrometry*

Grimm and Beauchamp developed a unique approach for producing ions from small liquid droplets by FIDI and introducing the ions into a mass spectrometer [39,40]. Neutral droplets placed in a sufficiently strong static electric field are known to elongate and develop two opposing conical tips that emit microjets of oppositely charged particles. The charged progeny particles then result in desolvated ions by mechanisms similar to those in conventional ESI [175], making it possible to analyse the droplet's chemical composition via MS. The key advantage of this technique is in its ability to simultaneously analyse the same droplet by both positive and negative ion MS. Practical applications of FIDI require a single mass spectrometer that is switchable between the positive and the negative ion mode operations. A stationary 1–2 mm droplet typically is formed at the tip of the capillary, exposed to a gas-phase reagent for a specified period of time, and then subjected to a high electric field to induce jetting (Figure 10). One of the jets is directed into a mass spectrometer for analysis. If ions of another polarity are analysed, the field direction is reversed.

The electric field required to induce jetting from a neutral droplet (E_c^0) is known as the 'Taylor limit' [176]. E_c^0 is related to the surface tension, σ, and droplet diameter, d, as shown in Equation (5) [40]:

$$E_c^0 \approx 1.625\sqrt{\frac{\sigma}{2\pi\varepsilon_0 d}} \tag{5}$$

For methanol droplets ($\sigma = 0.022$ N/m), the predicted Taylor limit is 1.0 MV/m for a 1-mm particle. The electric field required for FIDI presents certain experimental difficulties because it is close to the breakdown limit of air (~3 MV/m). As a result of this limitation, pure water droplets ($\sigma = 0.072$ N/m) cannot be easily investigated via FIDI. If the droplet carries charge, the

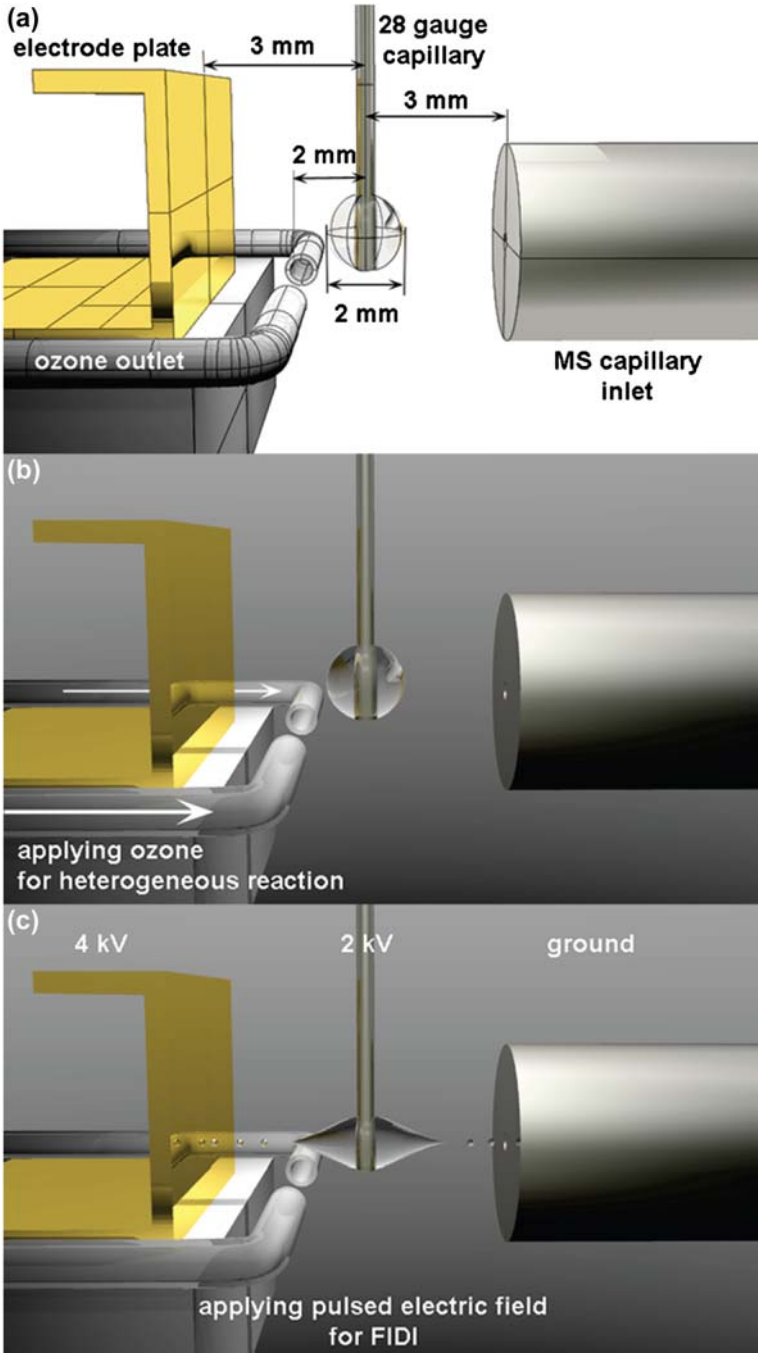

Figure 10. (Colour online) A FIDI experimental setup used for investigation of reactions between ozone and phospholipids on surfaces of liquid droplets. Reproduced with permission from Ref. [180].

critical field required to induce jetting is reduced and the droplet produces only one jet of progeny particles (Figure 11). When the droplet charge exceeds the Rayleigh limit (Equation (6)):

$$q_R = \sqrt{8\pi^2\sigma\varepsilon_0 d^3} \tag{6}$$

the droplet fission occurs spontaneously.

Reactions at the liquid–air interface can be conveniently investigated by exposing the droplet to gas-phase reactants for a short period of time, typically a few seconds, prior to turning on the electric field. This approach is especially useful for investigating interfacial chemistry of surface-active molecules because they tend to be enhanced [177,178] in the progeny droplets during droplet break-up. The utility of FIDI for studying chemistry at interfaces was demonstrated shortly after the initial development of the technique. Grimm and Beauchamp [179] were able to observe naphthalene-Ag^+ ions after exposing a water/methanol droplet containing dissolved silver ions to naphthalene vapour. In the same paper, they examined the mechanism of oleic acid ozonolysis by monitoring the products of the interfacial reaction between oleic acid and gas-phase ozone. In addition, they demonstrated that the method is suitable for locating the double bond position in phospholipids by studying the reaction between oleoyl-l-α-lysophosphatidic acid and ozone. Using FIDI, Kim

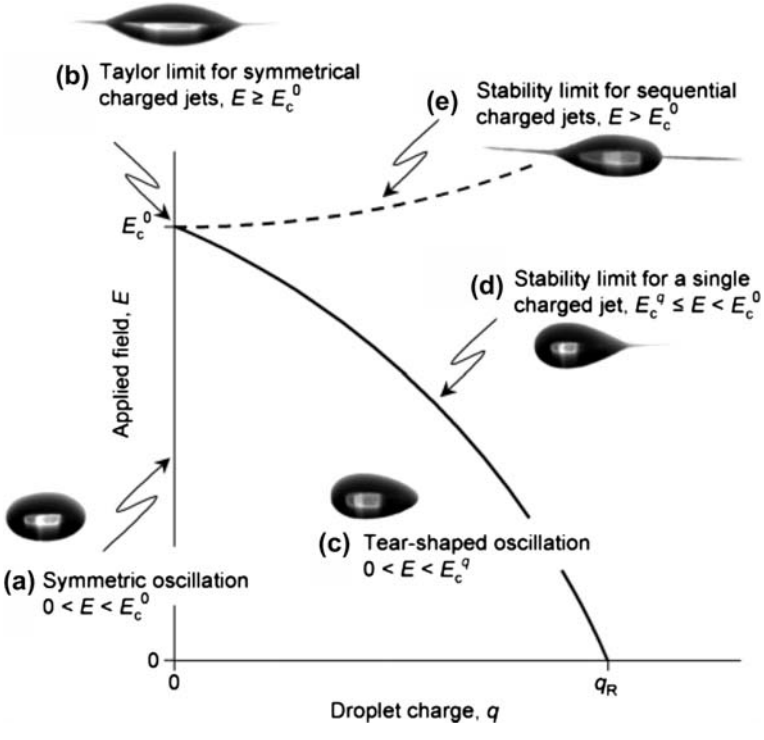

Figure 11. A schematic diagram showing different regions of stability for neutral and charged droplets placed in an electric field. As the droplet charge increases, the critical field required to induce FIDI is reduced, but jetting becomes asymmetric. Reproduced with permission from Ref. [40].

et al. [180] investigated heterogeneous ozonolysis of an unsaturated phospholipid, 1-palmitoyl-2-oleoyl-*sn*-phosphatidylglycerol (POPG), at the air–water/methanol interface. They were able to observe hydroxyhydroperoxide and secondary ozonide (SOZ = 1,2,4-trioxolane) products of ozonolysis, which are difficult to detect with traditional ESI-MS due to their low stability. As SOZs are not commonly produced in the aqueous ozonolysis of alkenes in the bulk, the observation of the SOZ product was attributed to a unique interfacial process. The same group also studied the reaction of ozone with a mixture of phospholipids, such as unsaturated POPG and saturated 1,2-dipalmitoyl-sn-phosphatidylglycerol or saturated 1,2-dipalmitoyl-sn-phosphatidylcholine and unsaturated 1-stearoyl-2-oleoyl-sn-phosphatidylcholine. The results were consistent with the phospholipids forming a uniformly mixed layer. With extensive ozonolysis, the unsaturated phospholipids formed more hydrophilic products and transitioned into the droplet, and only saturated phospholipids remained on the surface. Recently, Ko *et al.* applied FIDI-MS to studying interfacial reactions of cholesterol sulphate in a POPG layer with ozone [181]. They observed an epoxide of cholesterol sulphate as the major oxidation product. In light of the significant interest in chemical processes occurring at air–liquid interfaces, we can expect a number of new applications of FIDI and related methods (including the one described in the next section) to appear in the future.

4.2. *Mass spectrometric studies of the reactivity at the air–water interface in microdroplets*

In 2007, Enami *et al.* developed another novel mass spectrometric method that is intrinsically sensitive to the processes occurring at the droplet–air interface [41]. In this method, a solution is sprayed under pressure into a chamber through a grounded, stainless-steel capillary surrounded by a coaxial flow of a nebulising gas as shown in Figure 12. Because of the gas flow's large velocity (>200 m/s), the much slower liquid jet (~0.1 m/s) is quickly shredded into micrometer-sized droplets (microdroplets). With terminal velocities of the microdroplets in excess of 10 m/s, it takes less than 1 ms for the droplets to cross the orthogonal plume of a gas-phase reactant, such as ozone in the spraying chamber. Although the spray is neutral on the whole, some droplets carry positive or negative charge acquired as a result of normal statistical fluctuations in the number of charges per droplet [182]. As the charged droplets evaporate, they eventually reach the Rayleigh limit for Coulomb fission and produce progeny droplets and desolvated ions by mechanisms similar to ESI [175]. A mass spectrometer collects ions from the spray through an electrified pinhole. For example, in Figure 12, a negative potential is applied to the mass spectrometer entrance pinhole to extract positive ions from the gas flow. Due to the enhancement of the surface-active species in droplet fission processes, the mass spectrometer preferentially samples species that reside on the surface of the original microdroplets. It is the combination of the short gas–droplet exposure time and the bias toward detecting surface-active species that makes this method exquisitely sensitive to the reactions occurring at the gas–droplet interface. Furthermore, the observed ion signals are directly proportional to ion concentrations in the interfacial layers of the microjets prior to their break-up into microdroplets [183]. Numerous problems, ranging from oxidation of surfactants on water droplets by atmospheric oxidants to the fundamental issue of proton availability at the water–air interface, have been investigated with this approach [41,183–196]. Some of these studies are highlighted later herein.

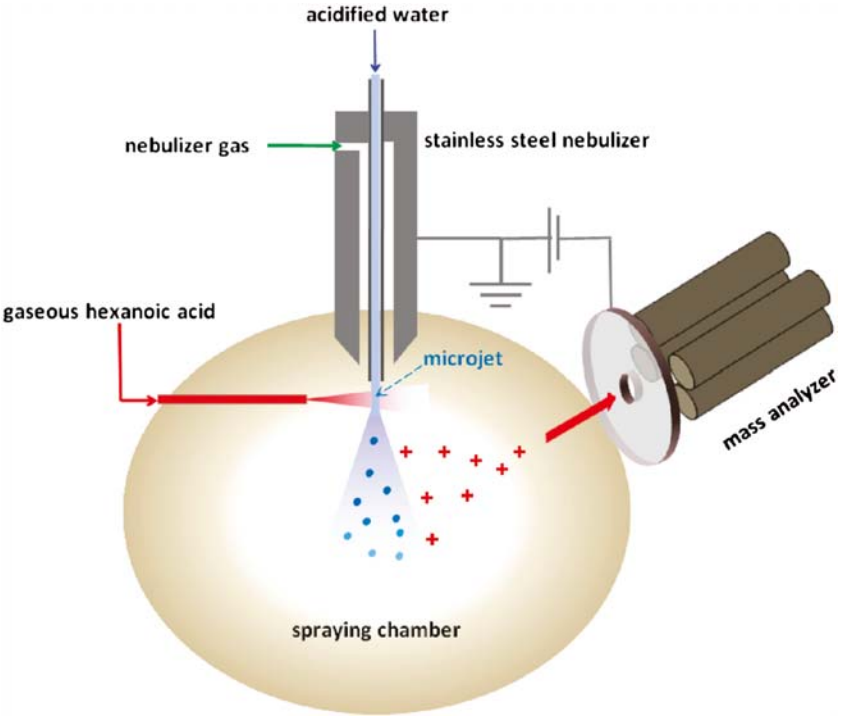

Figure 12. (Colour online) A schematic diagram of the setup for investigating chemistry occurring at the air–liquid interface of small droplets. Reproduced with permission from Ref. [191].

Compounds containing halogen atoms play an important role in the lower atmosphere, especially in coastal and marine environments where various halogen-containing molecules are produced by reactions between gas-phase air pollutants and sea salt particles [197]. Chemical processes involving bromine and iodine species are of special interest because of the high efficiency of these compounds in the catalytic destruction of ozone. Enami *et al.* [192] observed that oxidation of Br^- and Cl^- by ozone in liquid droplets is efficiently catalysed by I^-, a minor component of sea salt. In the proposed mechanism, I^- is oxidised by ozone to HOI, which reacts with X^- halogen ions via an IX_2^- intermediate, leading to a release of X_2 in the gas-phase and regeneration of I^- (X = Cl or Br). The presence of sulphate species in the droplet significantly affects the oxidation of I^- by ozone. Enami *et al.* [41] could directly observe previously postulated (but never observed) ISO_3^- and $IS_2O_3^-$ intermediates in reactions between microdroplets containing dissolved I^- and $S_2O_3^{2-}$ with ozone. They also demonstrated the relative reactivity of I^- and $S_2O_3^{2-}$ with ozone at the air–water interface was quite different from that in the bulk solution, an important test of the surface selectivity of their experimental method. Finally, Hayase *et al.* [194] found that aqueous surface oxidation of I^- by ozone is suppressed by the presence of phenols because of efficient competition between I^- and phenolates for ozone but is unaffected by common atmospheric compounds butanol and malonic acid. These results highlight the molecular specificity of the effects of surface-active organics on interfacial chemistry.

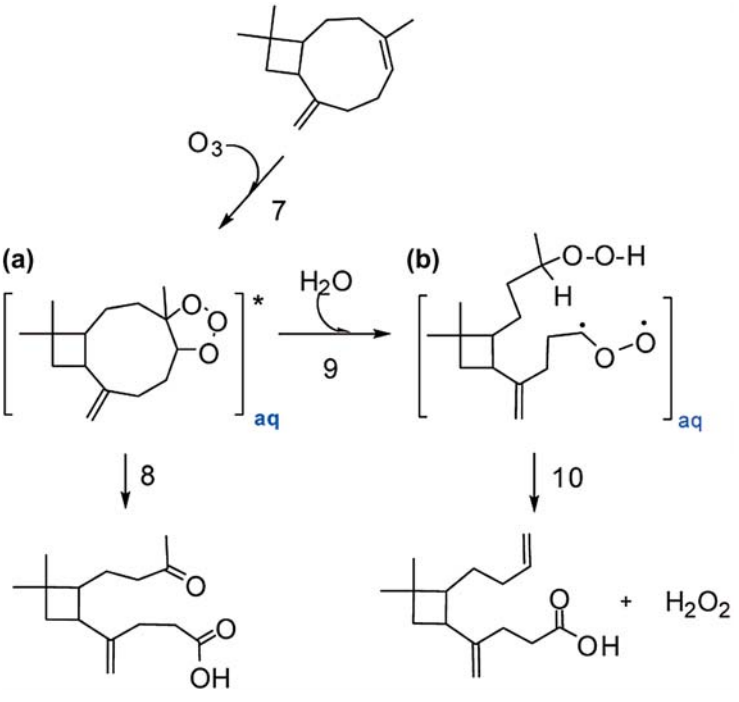

Figure 13. Proposed mechanism of oxidation of β-caryophyllene by ozone at the air–water interface. Reproduced with permission from Ref. [189].

A series of studies by the same research group explored air–water interface reactions between ozone and various organic compounds, including uric acid [184], ascorbic acid [185], glutathione [187], β-caryophyllene [189], phenol and α-tocopherol [186]. All of these studies have provided compelling evidence of unique chemical processes occurring at the air–water interface. For example, epoxide, peroxide and SOZ of uric acid could be directly observed in the experiments with the microdroplets, whereas ozonolysis of the bulk solution produced only epoxide and traces of peroxide. In addition, the rate of the surface uric acid + ozone reaction increased rapidly with pH, and it was independent of pH in the bulk from pH 4–7 [184]. Ozonolysis of β-caryophyllene [189] at the air–water interface was shown to occur faster and give rise to a distinctly different set of products than in the bulk water. Specifically, carboxylic acids, minor products of ozonolysis in bulk aqueous solution, were the major products believed to result from a reaction of the primary ozonide (POZ = 1,2,3-trioxolane) with interfacial water (Figure 13). Ozonolysis of ascorbic acid at the air–water interface below pH 5 was shown to result in a significant yield of SOZ, which was not present among the products of the ascorbic acid + ozone reaction in bulk water [185]. The efficient production of SOZ, a highly reactive peroxidic species, has significant epidemiological and toxicological implications because ascorbic acid is a key antioxidant present, for example, in epithelial lining fluids. Aqueous surface ozonolysis of another natural antioxidant, glutathione [187], converted its thiol, –SH, group into a sulfonic group, $-SO_3^-$. The relative reactivities of glutathione, ascorbic acid and uric acid toward gas-phase ozone did not

match those toward aqueous ozone in the bulk solution. These studies make it clear that the air–water interface provides a unique reaction media for ozone chemistry, different from both gas- and condensed-phase environments in terms of reaction rates and mechanisms. The air–water interface provides a similarly unique environment for reactions of other atmospheric oxidants, such as OH [198]. Therefore, extensions of these methods to other types of oxidants are desirable.

Another series of papers by the same group examined the availability of protons at the air–water interface and the efficiency of proton transfer to and from water through such an interface. Proton transfer equilibria are known to be dramatically sensitive to the solvation state of the ions involved. For example, hydronium ions readily protonate most organic compounds in the gas-phase, whereas only relatively strong bases can be protonated by a similar reaction in bulk water because of the high free energy of hydration of the hydronium ion relative to that of the protonated base. Enami *et al.* [183] used reactions between gas-phase trimethylamine (TMA), a compound with high gas-phase basicity (227 kcal/mol), and microdroplets with different bulk pH to probe the apparent availability of protons at the air–water interface. The 'titration curve' representing the signal of TMA-H^+ versus the bulk solution pH had an 'equivalence point' (i.e. the pH value below which the TMA-H^+ signal increased abruptly) at $pH_{bulk} = 3.8$. This was quite different from the 9.8 pK_a of TMA-H^+, the value reproduced in the same experiments by spraying pre-mixed solutions of TMA chloride with different initial pH. The authors concluded that hydronium ions are accessible to the gas-phase TMA species colliding with the surface of water microdroplets only below pH_{bulk} 4. In the presence of certain surface-active organic compounds, such as fulvic acid, the protonation could be achieved at a higher pH_{bulk}, suggesting that these organic molecules may act as proton donors instead of the hydronium ions [188]. A similar experiment also was conducted with n-hexanoic acid [191], the gas-phase basicity (187 kcal/mol) of which is closer to that of water (158 kcal/mol). Although the protonated form of hexanoic acid is a strong acid with a negative effective $pK_a < -3$, the authors observed protonation of the –C(O)OH group of hexanoic acid, resulting in $-C(OH)_2^+$ occurring at pH_{bulk} as high as 3–4. Stated differently, at $pH_{bulk} < 4$, the aqueous surface behaved as a 'superacid' with respect to the protonation of the molecules colliding with it. Because of the high kinetic isotope effect observed on H_2O vs. D_2O microjets, they surmised that protonation involves proton tunneling through the outermost layers of water and is controlled by both the reaction energetics and the dynamics of the proton tunneling process. A new twist to the story has been provided by a recent experiment, where aqueous microdroplets were exposed to HNO_3 [196]. Although HNO_3 is strong acid, it did not produce NO_3^- upon collisions with water surfaces at neutral pH_{bulk} unless the solution already contained a small amount of other ions. Density functional calculations by the authors suggested that anions in the surface layers of the droplet electrostatically assist in withdrawing the proton away from NO_3^-. It should be clear from these examples that the proton transfer processes at the interfaces may follow distinctly different – and not always intuitive – predictable pathways.

Perhaps the most remarkable example of a unique proton transfer process at the air–water interface was the observation that isoprene, the second most important organic molecule emitted by the biosphere (after methane), is capable of protonation and cationic oligomerisation during collisions with mildly acidic ($pH_{bulk} < 4$) droplets [190]. It is known that highly acidic surfaces such as >80 wt.% sulphuric acid take up isoprene efficiency and convert it into

polymeric products [199]. It appears that a similar process may take place under more environmentally relevant conditions. This process, estimated to occur with an effective uptake coefficient of $\sim 10^{-6}$ (one out of a million gas–aqueous surface collisions), has the potential to contribute to nighttime removal of isoprene by thin water films on various environmental surfaces, including the forest canopy and aerosol particles. If such interface-specific processes turn out to be universally applicable to all biogenic terpenoids, we will have to reconsider their emission inventories, as well as the mechanisms of SOA formation, from such compounds.

4.3. *Laser abblation mass spectrometry of levitated and supported droplets*

Laser desorption/ionisation (LDI) of liquid droplets has many advantages for qualitative analysis of the mixture components compared to LDI on solids. In contrast to LA from solids, liquids represent a more homogenous sample, and the spot ablated by the laser 'heals' quickly. Therefore, each subsequent laser pulse in effect probes a fresh sample. Jorabchi *et al.* [42] examined the enhancement of matrix-assisted laser desorption ionisation (MALDI) signal from immobilised liquid droplets in the presence of corona ions. In that study, a microliter droplet was placed on a conducting stainless-steel or on a non-conducting Teflon support between an entrance tube of a mass spectrometer and a corona needle. A pulsed nitrogen laser was focused on the droplet from above. Using a clever way of timing the corona discharge voltage with respect to the laser pulses, they were able to demonstrate that ion enhancement was not a result of postdesorption ionisation of neutral compounds by the corona ions. Rather, it was a result of charging the electrically isolated droplet. The charged droplet was distorted in the applied field from the corona tip, which increased the ion formation efficiency at the droplet surface closest to the mass spectrometer entrance. The main advantage of this mechanism, referred to as 'CALDI', by the authors, is that it requires a significantly lower external field compared to the standard AP-MALDI or ESI methods.

Westphall *et al.* [200] took advantage of CALDI's lower electric field requirements in what appears to be the first MS study of acoustically levitated microdroplets. Acoustic levitation is ideally suited for CALDI because this technique depends only on the density of the levitated particle, not on its size or charge. Charging the droplet prior to the LDI pulse was shown to be critical for the mass spectral detection of ions. In fact, no ions could be observed in these experiments if the droplet was not initially charged. Figure 14 illustrates the optimal timing of the experiment, in which the droplet is first charged to the highest possible level with the corona discharge, then allowed to equilibrate in the acoustic trap, and finally subjected to the LDI pulse. The entire timing sequence was repeated at the repetition rate of the laser (20 Hz in these experiments). The resulting mass spectra of oligopeptides contained singly charged protonated and sodiated ions with minimal fragmentation.

In the two previously described studies, the UV laser used for desorption/ionisation required significant amounts of chromophoric compounds and diethanolamine as part of the MALDI matrix, which suppressed partitioning of analytes to the surface. Jorabchi and Smith [201] described an alternative approach, in which a relatively low-power IR laser was used for preferential desorption of surface-active analytes from a droplet resting on a stainless-steel capillary followed by postionisation with a methanol/formic acid electrospray. They demonstrated the surface bias of this method by an observation that more surface-active molecules were depleted from the droplet faster as the droplet was subjected to repeated IR

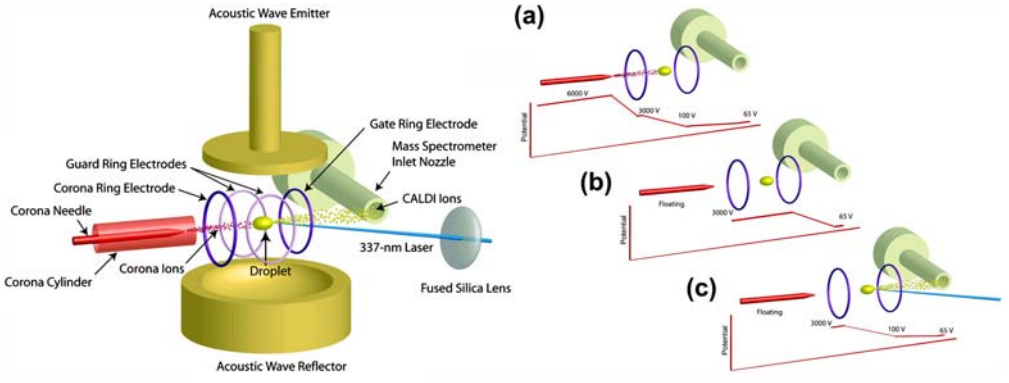

Figure 14. (Colour online) Schematic diagram of the setup for taking CALDI mass spectra of acoustically levitated particles and the timing sequence of the experiment involving charging the droplet, equilibration step and LDI step. Reproduced with permission from Ref. [200].

desorption pulses. These results were rationalised using a model that related the surface partitioning coefficients with the observed decay rates of the ion signals. The authors found a correlation between the surface partitioning and the phase partitioning coefficients on a C_{18} HPLC column. Thus, the approach may become a viable separation tool for organic analytes in microdroplets.

4.4. *Ion-mobility studies of nanodroplets*

IMS [202] is a well-established technique based on separating ions by their mobility through a buffer gas. Mobility Z ($cm^2\,V^{-1}\,s^{-1}$) is defined as a proportionality constant between the terminal velocity of the ion, v ($cm\,s^{-1}$), and the electrostatic field, E ($V\,cm^{-1}$), as shown in Equation (7):

$$v = Z \times E \tag{7}$$

In the low-field limit, the mobility is inversely proportional to the product of the buffer gas density and the collisional cross section, which, in turn, depends on the ion's size and shape. A typical IMS instrument contains a pulsed ion source, linear drift region and suitable ion detector. IMS instruments often are coupled to quadrupole, ion trap or TOF mass spectrometers to enable precise determination of the masses of ions exiting the drift region [203]. IMS-MS methods traditionally have been applied to comparatively small molecular ions, cluster ions and biomolecules, generally less than 1 nm in size [203,204]. Larger particles, with diameters exceeding several nanometers, are normally sized with mobility instruments of a very different design [205], known as 'differential mobility analysers' (DMAs). The fundamental difference between IMS and DMA instruments is that the former separate packets of ions in time, whereas the latter separate continuous streams of ions or charged particles in space. A standard DMA consists of a continuous particle source, particle charger/neutraliser, cylindrical drift region and a particle detector, either a condensation particle counter or an electrometer. Commercial

DMAs, such as those produced by TSI Inc. (Shoreview, MN), work best for particles ranging from about 5 to 1000 nm in size. A number of studies coupled traditional ESI sources with DMA-type instruments to investigate chemistry of nanoparticles in solution. The readers are referred to a recent review by Guha *et al.* [206], which provides an excellent overview of this research area and is not covered in this article.

The size range of 1–5 nm traditionally has been difficult to access with conventional IMS and DMA instruments. However, particles in this size range are critical in homogeneous nucleation of atmospheric aerosols and in emerging nanoparticle technologies. In recent years, significant efforts have been expended to morph the IMS-MS and DMA approaches to extend their capabilities and provide new tools for nanoparticle characterisation. For example, the Fernandez de la Mora group incorporated a high-resolution parallel-plate DMA, shown schematically in Figure 15, into atmospheric pressure ionisation sources of various types of mass spectrometers and described the design criteria for achieving both high ion transmission and high resolving power of the DMA [207]. For smaller particle sizes, the resolving power of DMAs is primarily limited by diffusion perpendicular to the intended direction of the drift. To overcome the diffusion limitations, the DMA had to be operated under the conditions of high Reynolds numbers, where any design fault would result in turbulent flows. The authors were able to achieve a resolving power in mobility ($Z/\Delta Z$) in excess of 50 while keeping the charged particle transmission greater than 50%.

The DMA-MS approach developed by the de la Mora group made it possible to quickly and sensitively obtain impressively large amounts of two-dimensional mobility-mass data. For example, Hogan and de la Mora investigated the evaporation of ions from ionic liquid-acetonitrile nanodrops [208] and evaporation of ion pairs from charged clusters of ionic liquids [209], while Larriba *et al.* [210] examined the relationship between the mobility and the volume of nanodrops of ionic liquids with diameters up to 3 nm. A sample mobility-mass spectrum of particles produced by electrospraying 1-ethyl-3-methylimidazolium tetrafluoroborate (EMI-BF_4) is reproduced in Figure 16. The observed peaks correspond to ions $(EMI^+)_z(EMI\text{-}BF_4)_n$. The *m/z*-axis has been converted into *n/z*-axis in the figure, where *n* is the number of the EMI-BF_4 ion pairs per particle and *z* is the particle's charge. For singly charged clusters, the observed *n* ranges from 0 to more than 40. Even larger values of *n* can be observed in multiply charged particles. The peaks are narrower in the *n/z* dimension because of the higher resolving power of the mass spectrometer ($m/\Delta m \sim 10^4$) compared to that of the DMA ($Z/\Delta Z \sim 50$).

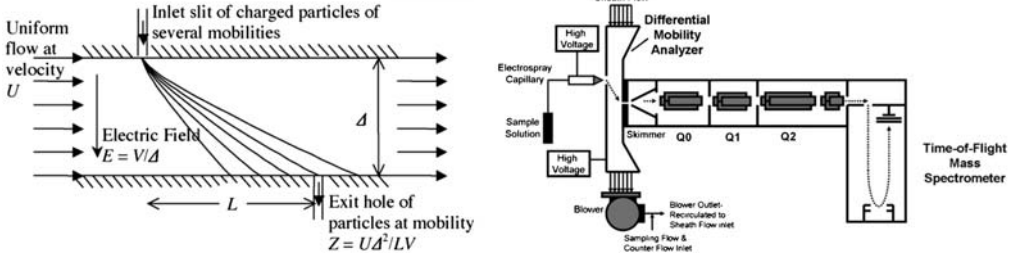

Figure 15. Schematic diagram of separation of charged particles by their mobility in a parallel plate DMA and a diagram of a practical DMA-MS instrument. Reproduced with permission from Refs. [207,208].

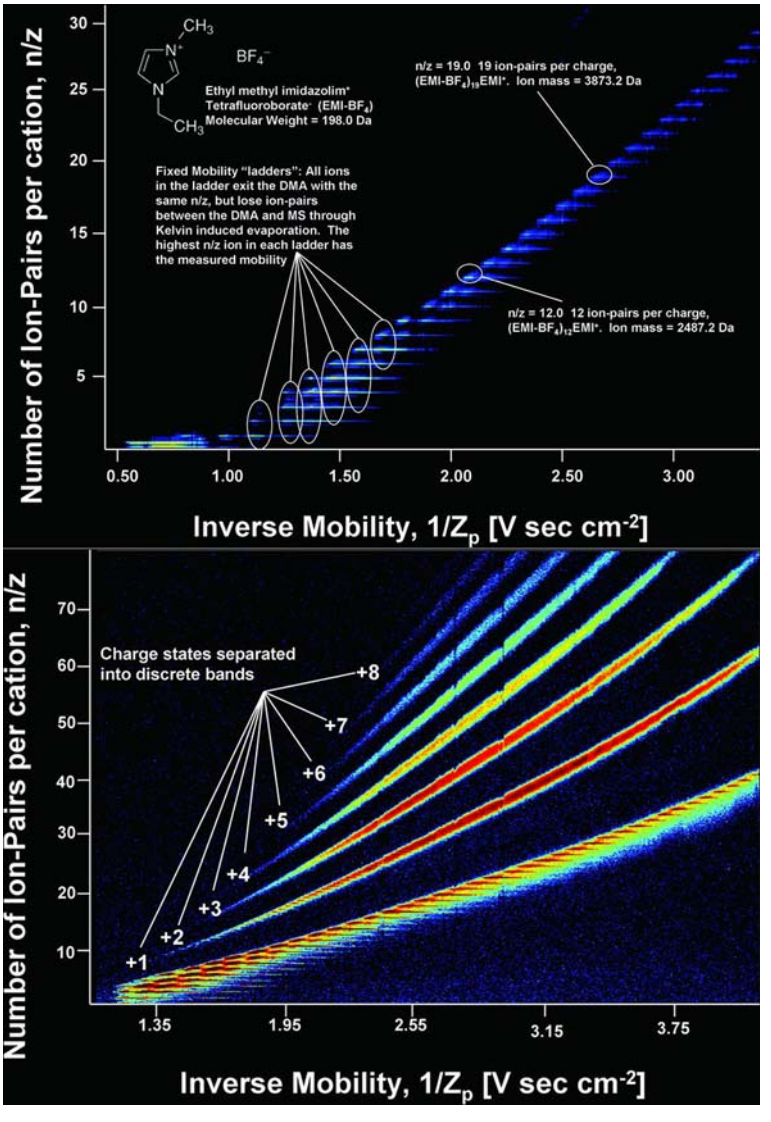

Figure 16. (Colour online) A mobility-mass spectrum of particles generated by electrospraying a solution of ionic liquid EMI-BF_4 in acetonitrile. Only singly charged ions $EMI^+(EMI\text{-}BF_4)_n$ are visible in the top panel. The intensity scale has been adjusted in the bottom panel to better showcase the multiply charged ions $(EMI^+)_z(EMI\text{-}BF_4)_n$. Reproduced with permission from Ref. [210].

Such a mobility-mass data-set is impressively rich with information. For example, the particle densities can be directly calculated from the observed masses and mobilities using the Stokes–Mulliken equation, which relates mobility to the volume-equivalent diameter and accounts for the finite size of the gas-phase molecules colliding with the particle [211]. The apparent particle densities approach bulk values for particles with diameters in excess of

1.5 nm [210]. The apparent density is significantly reduced for smaller particles because particles deviate from spherical shapes as they approach molecular dimensions. In addition, the importance of the ion-induced dipole interactions in particle–molecule collisions becomes greater at smaller particle sizes. Both effects decrease the particle mobility relative to that expected for a spherical object drifting through a flow of non-polarisable molecules.

The dynamics of droplet evaporation have been examined using mobility-mass measurements. For each mobility value, several *n/z* peaks are observed for singly charged ions ($z = 1$) in Figure 16 instead of a single peak. This has been interpreted [209] as a result of ion-pair evaporation from the ionic liquid droplets occurring in the ion guide of the mass spectrometer (region Q_0 in Figure 15) as a result of RF heating. Although ionic liquids generally are viewed as involatile, the droplet surface's high degree of curvature enables evaporation of the EMI-BF_4 ion pairs via the Kelvin effect (ion-pair evaporation from aerosolised ionic liquids also has been observed [212] using VUV photoionisation of the free ion pairs). Evaporation of ions from multiply charged droplets also was observed with the most common process corresponding to the loss of (EMI^+)(EMI-BF_4). The highly efficient evaporation of the droplets makes it challenging to investigate more volatile nanodroplets made of water or common organic solvents using this technique. However, this limitation likely can be overcome in the future by using a buffer gas maintained at a predefined RH, similar to the approach used in tandem DMA instruments designed to quantify hygroscopic growth of particles [213].

5. Summary and outlook

Recent developments of MS-based techniques highlighted in this review facilitate opportunities for improved understanding of the mechanisms and kinetics of reactions affecting physical and chemical properties of ambient particles and droplets. Although the MS techniques reviewed here are not universally applicable to all types of particles, and some are limited only to laboratory studies by virtue of the instrumental design, the broad arsenal of the available MS methods makes it possible to pick one or several methods tailored to a specific application. For example, ambient surface ionisation techniques enable direct analysis of particles collected on substrates without special sample pre-treatment. When coupled with HR-MS, these techniques can be used for detailed characterisation of the chemical composition of the inherently complex SOA samples. This capability is particularly important for understanding mechanisms of heterogeneous reactions of SOA with common atmospheric gases responsible for chemical ageing of SOA in the atmosphere. Furthermore, reactive analysis may be used for quantification of reaction products in complex mixtures. Although a variety of ambient surface ionisation techniques developed in the last decade have been used in forensics, biological materials analysis, counterfeit drug detection, chemical imaging and other applications, only a few of these methods have been applied for characterisation of aerosol samples. This presents a clear opportunity for future developments in the field of chemical analysis of aerosol samples.

Several vacuum-based techniques traditionally used for characterisation of mineral surfaces and soil samples (e.g. NanoSIMS and LA-ICPMS) show great potential for depth profiling and imaging of individual particles on substrates. Recent developments in SIMS instrumentation [43] have resulted in improved sensitivity and better spatial resolution, which enabled the first high-resolution elemental mapping of heterogeneous inorganic particles. Combined with depth profiling capabilities, this technique may be used in the future for 3D chemical imaging of individual particles on substrates. Although images of individual

particles deposited on the substrates may be affected by transformations of particle morphologies upon sample collection, these effects can be minimised by gentle deposition of charged particles using ion soft landing [214–216] that can be further developed for particle deposition. Alternatively, the advent of novel coherent light source facilities based on X-ray free electron laser technology has opened up an additional unique opportunity for on-the-fly imaging and mass spectrometric characterisation of individual particles [217].

Ambient liquid droplets are unique reactive vessels, in which both the rates and pathways of chemical reactions may be dramatically different from the bulk solution. For example, rates of some organic reactions are enhanced by several orders of magnitude when the reaction occurs in a submicron-sized droplet. MS approaches summarised in this review are ideally suited for understanding chemistry on droplets with sizes spanning several orders of magnitude (from nanometers to millimeters in diameter). These techniques provide unique insights on the surface chemistry of microdroplets. For example, MS has been used for examining the availability of protons and proton transfer phenomena at the air–water interface. These studies demonstrated that at relatively mild acidic pH, the aqueous surface behaves as a superacid as reflected by the unexpectedly efficient protonation of gas-phase molecules impinging on the surface of the droplet. The observation of ozone + olefin reaction products that do not readily form in the bulk is another example of unusual chemistry occurring at the air–water interface that can now be investigated using emerging MS methods. These examples highlight exciting future opportunities in the field of droplet MS. In addition, combining experimental data with molecular dynamics modelling may have a significant impact both on understanding chemistry in cloud and fog droplets and toward a fundamental understanding of physical chemistry underlying ambient ionisation techniques.

This review also makes the point that gathering comprehensive information on the chemical composition, reactivity and transformations of environmental particles and surfaces is an especially challenging task because no single method of analytical chemistry is capable of providing the full range of necessary information. For example, methods of single-particle MS analysis may probe and sometimes even visualise particle morphology and internal structure at nanometer scale. However, they provide limited information on particle molecular content. HR-MS interfaced with ambient surface ionisation approaches may provide detailed information on molecular content of organic particles and surfaces, but these methods acquire integrated signal from an ensemble of particles and eliminate knowledge of particle individual composition. Therefore, the application of complementary analytical methods is needed to provide comprehensive information, ranging from microscopy-level details of individual particles to advanced molecular characterisation of complex organics comprising particulate matter.

Acknowledgements

The authors acknowledge previous and ongoing support for their research projects described in this review: US Department of Energy's (DOE) Office of Basic Energy Sciences, Division of Chemical Sciences, Geosciences and Biosciences (JL); DOE's Office of Biological and Environmental Research (BER) Atmospheric System Research programme and the W.R. Wiley Environmental Molecular Sciences Laboratory's (EMSL) intramural research and development programme (AL); and the National Science Foundation grants AGS-1227579 and CHE-0909227 (SAN). Additionally, JL and AL acknowledge a multi-program Chemical Imaging Initiative funded through Pacific Northwest National Laboratory's (PNNL) Laboratory Directed Research and Development programme that allowed compilation of this review. EMSL is a national scientific user facility sponsored by DOE-BER and

located at PNNL. PNNL is operated by Battelle for the DOE under Contract No. DE-AC05-76RL01830.

References

[1] N.O.A. Kwamena, J. Buajarern, and J.P. Reid, J. Phys. Chem. A **114**, 5787 (2010).
[2] A.K. Bertram, S.T. Martin, S.J. Hanna, M.L. Smith, A. Bodsworth, Q. Chen, M. Kuwata, A. Liu, Y. You, and S.R. Zorn, Atmos. Chem. Phys. **11**, 10995 (2011).
[3] B.J. Finlayson-Pitts, Phys. Chem. Chem. Phys. **11**, 7760 (2009).
[4] Y. Rudich, N.M. Donahue, and T.F. Mentel, Annu. Rev. Phys. Chem. **58**, 321 (2007).
[5] M.E. Monge, T. Rosenørn, O. Favez, M. Müller, G. Adler, A. Abo Riziq, Y. Rudich, H. Herrmann, C. George, and B. D'Anna, Proc. Natl. Acad. Sci. **109**, 6840 (2012).
[6] P. Kulkarni, P.A. Baron and K. Willeke, editors. *Aerosol Measurement* (John Wiley & Sons, Hoboken, NJ, 2011).
[7] R. Signorell and J.P. Reid, editors. *Fundamentals and Applications in Aerosol Spectroscopy* (Taylor and Francis Books, Inc., CRC Press, Boca Raton, FL, 2011).
[8] H.R. Pruppacher and J.D. Klett, *Microphysics of Clouds and Precipitation*. 2nd ed. (Kluwer Academic, Boston, MA, 1997).
[9] M.O. Andreae and D. Rosenfeld, Earth-Sci. Rev. **89**, 13 (2008).
[10] J.M. Waldman, J.W. Munger, D.J. Jacob, R.C. Flagan, J.J. Morgan, and M.R. Hoffmann, Science **218**, 677 (1982).
[11] J.P. Reid and R.M. Sayer, Chem. Soc. Rev. **32**, 70 (2003).
[12] D.J. Donaldson and K.T. Valsaraj, Environ. Sci. Technol. **44**, 865 (2010).
[13] B. Ervens, B.J. Turpin, and R.J. Weber, Atmos. Chem. Phys. **11**, 11069 (2011).
[14] D.J. Donaldson and V. Vaida, Chem. Rev. **106**, 1445 (2006).
[15] M.R. Canagaratna, J.T. Jayne, J.L. Jimenez, J.D. Allan, M.R. Alfarra, Q. Zhang, T.B. Onasch, F. Drewnick, H. Coe, A. Middlebrook, A. Delia, L.R. Williams, A.M. Trimborn, M. J. Northway, P.F. DeCarlo, C.E. Kolb, P. Davidovits, and D.R. Worsnop, Mass Spectrom. Rev. **26**, 185 (2007).
[16] K.A. Pratt and K.A. Prather, Mass Spectrom. Rev. **31**, 1 (2012).
[17] K.A. Pratt and K.A. Prather, Mass Spectrom. Rev. **31**, 17 (2012).
[18] S.A. Nizkorodov, J. Laskin, and A. Laskin, PCCP **13**, 3612 (2011).
[19] J. Zahardis, S. Geddes, and G.A. Petrucci, Anal. Chem. **83**, 2409 (2011).
[20] A. Zelenyuk and D. Imre, Int. Rev. Phys. Chem. **28**, 309 (2009).
[21] K. Hartonen, T. Laitinen, and M.L. Riekkola, TrAC, Trends Anal. Chem. **30**, 1486 (2011).
[22] T. Hoffmann, R.J. Huang, and M. Kalberer, Anal. Chem. **83**, 4649 (2011).
[23] Z.Y. Zhou, H.J. Guo, and F. Qi, TrAC, Trends Anal. Chem. **30**, 1400 (2011).
[24] B.R. Bzdek, M.R. Pennington, and M.V. Johnston, J. Aerosol Sci. (in press). <http://dx.doi.org/10.1016/j.jaerosci.2012.1005.1001>.
[25] A. Laskin, J. Laskin, and S.A. Nizkorodov, Environ. Chem. **9**, 163 (2012).
[26] C.E. Kolb and D.R. Worsnop, Annu. Rev. Phys. Chem. **63**, 471 (2012).
[27] T. Reemtsma, J. Chromatogr. A **1216**, 3687 (2009).
[28] R.G. Cooks, Z. Ouyang, Z. Takats, and J.M. Wiseman, Science **311**, 1566 (2006).
[29] G.A. Harris, L. Nyadong, and F.M. Fernandez, Analyst **133**, 1297 (2008).
[30] A. Venter, M. Nefliu, and R.G. Cooks, TrAC, Trends Anal. Chem. **27**, 284 (2008).
[31] H.W. Chen, G. Gamez, and R. Zenobi, J. Am. Soc. Mass. Spectrom. **20**, 1947 (2009).
[32] R.M. Alberici, R.C. Simas, G.B. Sanvido, W. Romao, P.M. Lalli, M. Benassi, I.B.S. Cunha, and M.N. Eberlin, Anal. Bioanal. Chem. **398**, 265 (2010).
[33] G.A. Harris, A.S. Galhena, and F.M. Fernandez, Anal. Chem. **83**, 4508 (2011).

[34] J. Laskin, A. Laskin, P.J. Roach, G.W. Slysz, G.A. Anderson, S.A. Nizkorodov, D.L. Bones, and L.Q. Nguyen, Anal. Chem. **82**, 2048 (2010).
[35] P.J. Roach, J. Laskin, and A. Laskin, Analyst. **135**, 2233 (2010).
[36] E.A. Bruns, V. Perraud, J. Greaves, and B.J. Finlayson-Pitts, Anal. Chem. **82**, 5922 (2010).
[37] L.A. Doezema, T. Longin, W. Cody, V. Perraud, M.L. Dawson, M.J. Ezell, J. Greaves, K.R. Johnson, and B.J. Finlayson-Pitts, Rsc Adv. **2**, 2930 (2012).
[38] S.J. Fuller, Y. Zhao, S.S. Cliff, A.S. Wexler, and M. Kalberer, Anal. Chem. (2012).
[39] R.L. Grimm and J.L. Beauchamp, J. Phys. Chem. B **107**, 14161 (2003).
[40] R.L. Grimm and J.L. Beauchamp, J. Phys. Chem. B **109**, 8244 (2005).
[41] S. Enami, C.D. Vecitis, J. Cheng, M.R. Hoffmann, and A.J. Colussi, J. Phys. Chem. A **111**, 13032 (2007).
[42] K. Jorabchi, M.S. Westphall, and L.M. Smith, J. Am. Soc. Mass. Spectrom. **19**, 833 (2008).
[43] J.S. Fletcher and J.C. Vickerman, Anal. Chem. (2012).
[44] R. Hergenroder, O. Samek, and V. Hommes, Mass Spectrom. Rev. **25**, 551 (2006).
[45] R.E. Russo, X.L. Mao, H.C. Liu, J. Gonzalez, and S.S. Mao, Talanta **57**, 425 (2002).
[46] J. Pisonero, J. Koch, M. Wälle, W. Hartung, N.D. Spencer, and D. Günther, Anal. Chem. **79**, 2325 (2007).
[47] D. Weibel, S. Wong, N. Lockyer, P. Blenkinsopp, R. Hill, and J.C. Vickerman, Anal. Chem. **75**, 1754 (2003).
[48] G.J. Van Berkel, S.P. Pasilis, and O. Ovchinnikova, J. Mass Spectrom. **43**, 1161 (2008).
[49] D.R. Ifa, C.P. Wu, Z. Ouyang, and R.G. Cooks, Analyst. **135**, 669 (2010).
[50] D.J. Weston, Analyst **135**, 661 (2010).
[51] X.X. Ma, S.C. Zhang, and X.R. Zhang, TrAC, Trends Anal. Chem. **35**, 50 (2012).
[52] Z. Takats, J.M. Wiseman, B. Gologan, and R.G. Cooks, Science. **306**, 471 (2004).
[53] Z. Takáts, J.M. Wiseman, and R.G. Cooks, J. Mass Spectrom. **40**, 1261 (2005).
[54] A.B. Costa and R.G. Cooks, Chem. Commun. 3915 (2007). doi:3910.1039/B710511H.
[55] A.B. Costa and R.G. Cooks, Chem. Phys. Lett. **464**, 1 (2008).
[56] V. Frankevich, R.J. Nieckarz, P.N. Sagulenko, K. Barylyuk, R. Zenobi, L.I. Levitsky, A.Y. Agapov, T.Y. Perlova, M.V. Gorshkov, and I.A. Tarasova, Rapid Commun. Mass Spectrom. **26**, 1567 (2012).
[57] M.C. Wood, D.K. Busby, and P.B. Farnsworth, Anal. Chem. **81**, 6407 (2009).
[58] J. Laskin, B.S. Heath, P.J. Roach, L. Cazares, and O.J. Semmes, Anal. Chem. **84**, 141 (2012).
[59] J.B. Fenn, M. Mann, C.K. Meng, S.F. Wong, and C.M. Whitehouse, Science **246**, 64 (1989).
[60] F.M. Green, T.L. Salter, P. Stokes, I.S. Gilmore, and G. O'Connor, Surf. Interface Anal. **42**, 347 (2010).
[61] H. Chen, M. Li, Y.P. Zhang, X. Yang, J.J. Lian, and J.M. Chen, J. Am. Soc. Mass. Spectrom. **19**, 450 (2008).
[62] M. Li, H. Chen, B.F. Wang, X. Yang, J.J. Lian, and J.M. Chen, Int. J. Mass Spectrom. **281**, 31 (2009).
[63] M. Li, H. Chen, X. Yang, J.M. Chen, and C.L. Li, Atmos. Environ. **43**, 2717 (2009).
[64] T.B. Nguyen, J. Laskin, A. Laskin, and S.A. Nizkorodov, Environ. Sci. Technol. **45**, 6908 (2011).
[65] T.B. Nguyen, P.B. Lee, K.M. Updyke, D.L. Bones, J. Laskin, A. Laskin, and S.A. Nizkorodov, J. Geophys. Res. Atm. **117**, D01207 (2012). doi:01210.01029/02011jd016944.
[66] T.B. Nguyen, P.J. Roach, J. Laskin, A. Laskin, and S.A. Nizkorodov, Atmos. Chem. Phys. **11**, 6931 (2011).
[67] R.E. O'Brien, A. Laskin, J. Laskin, S. Liu, R. Weber, L.M. Russell, and A.H. Goldstein, Atmos. Environ. (submitted for publication).
[68] R.E. O'Brien, T.B. Nguyen, A. Laskin, J. Laskin, P.L. Hayes, S. Liu, J.L. Jimenez, L.M. Russell, S.A. Nizkorodov, and A.H. Goldstein, J. Geophys. Res. Atm. (submitted for publication).

[69] P.J. Roach, J. Laskin, and A. Laskin, Anal. Chem. **82**, 7979 (2010).
[70] J. Laskin, P.A. Eckert, P.J. Roach, B.S. Heath, S.A. Nizkorodov, and A. Laskin, Anal. Chem. **84**, 7179 (2012).
[71] D.L. Bones, D.K. Henricksen, S.A. Mang, M. Gonsior, A.P. Bateman, T.B. Nguyen, W.J. Cooper, and S.A. Nizkorodov, J. Geophys. Res. Atm. 115, D05203 (2010). doi:05210.01029/02009jd012864.
[72] K.M Updyke, T.B. Nguyen, and S.A. Nizkorodov, Atmos. Environ. (accepted for publication).
[73] T. Koop, J. Bookhold, M. Shiraiwa, and U. Poschl, PCCP **13**, 19238 (2011).
[74] T.D. Vaden, D. Imre, J. Beranek, M. Shrivastava, and A. Zelenyuk, Proc. Natl. Acad. Sci. **108**, 2190 (2011).
[75] V. Perraud, E.A. Bruns, M.J. Ezell, S.N. Johnson, Y. Yu, M.L. Alexander, A. Zelenyuk, D. Imre, W.L. Chang, D. Dabdub, J.F. Pankow, and B.J. Finlayson-Pitts, Proc. Natl. Acad. Sci. **109**, 2836 (2012).
[76] P.A. Eckert, P.J. Roach, A. Laskin, and J. Laskin, Anal. Chem. **84**, 1517 (2012).
[77] H. Chen, I. Cotte-Rodriguez, and R.G. Cooks, Chem. Commun. 597 (2006).
[78] C.P. Wu, D.R. Ifa, N.E. Manicke, and R.G. Cooks, Anal. Chem. **81**, 7618 (2009).
[79] A.M. Gaddis, R. Ellis, and G.T. Currie, Nature **191**, 1391 (1961).
[80] A.S. Stachissini and L. Doamaral, J. Org. Chem. **56**, 1419 (1991).
[81] M. Girod, E. Moyano, D.I. Campbell, and R.G. Cooks, Chem. Sci. **2**, 501 (2011).
[82] A.K. Badu-Tawiah, D.I. Campbell, and R.G. Cooks, J. Am. Soc. Mass. Spectrom. **23**, 1077 (2012).
[83] A.K. Badu-Tawiah, J. Cyriac, and R.G. Cooks, J. Am. Soc. Mass. Spectrom. **23**, 842 (2012).
[84] C.N. McEwen, R.G. McKay, and B.S. Larsen, Anal. Chem. **77**, 7826 (2005).
[85] M.J.P. Smith, N.R. Cameron, and J.A. Mosely, Analyst **137**, 4524 (2012).
[86] E.A. Bruns, J. Greaves, and B.J. Finlayson-Pitts, J. Phys. Chem. A **116**, 5900 (2012).
[87] C.D. Cappa, E.R. Lovejoy, and A.R. Ravishankara, J. Phys. Chem. A **111**, 3099 (2007).
[88] S. Trimpin, J. Mass Spectrom. **45**, 471 (2010).
[89] B.X. Wang, C.B. Lietz, E.D. Inutan, S.M. Leach, and S. Trimpin, Anal. Chem. **83**, 4076 (2011).
[90] H. Chen, A. Venter, and R.G. Cooks, Chem. Commun. 2042 (2006).
[91] H. Zhang, J.D. Surratt, Y.H. Lin, J. Bapat, and R.M. Kamens, Atmos. Chem. Phys. **11**, 6411 (2011).
[92] M.M. Nudnova, L. Zhu, and R. Zenobi, Rapid Commun. Mass Spectrom. **26**, 1447 (2012).
[93] J. Ho, M.K. Tan, D.B. Go, L.Y. Yeo, J.R. Friend, and H.C. Chang, Anal. Chem. **83**, 3260 (2011).
[94] S. Guenther, K.C. Schafer, J. Balog, J. Denes, T. Majoros, K. Albrecht, M. Toth, B. Spengler, and Z. Takats, J. Am. Soc. Mass. Spectrom. **22**, 2082 (2011).
[95] B. Hu, X.L. Zhang, M. Li, X.J. Peng, J. Han, S.P. Yang, Y.Z. Ouyang, and H.W. Chen, Analyst **136**, 4977 (2011).
[96] A. Benninghoven, F.G. Rudenauer and H.W. Werner, *Secondary Ion Mass Spectrometry: Basic Concepts, Instrumental Aspects, Applications and Trends* (Wiley, New York, NY, 1987).
[97] R.J. Day, S.E. Unger, and R.G. Cooks, Anal. Chem. **52**, A557 (1980).)
[98] A. Benninghoven, Angew. Chem. Int. Ed. **33**, 1023 (1994).
[99] R.N.S. Sodhi, Analyst **129**, 483 (2004).
[100] H. Tervahattu, J. Juhanoja, and K. Kupiainen, J. Geophys. Res. Atm. **107**, 4319 (2002). doi:4310.1029/2001jd001403.
[101] A. Laskin, D.J. Gaspar, W.H. Wang, S.W. Hunt, J.P. Cowin, S.D. Colson, and B.J. Finlayson-Pitts, Science **301**, 340 (2003).
[102] R.E. Peterson and B.J. Tyler, Appl. Surf. Sci. **203**, 751 (2003).

[103] H. Tervahattu, J. Juhanoja, V. Vaida, A.F. Tuck, J.V. Niemi, K. Kupiainen, M. Kulmala, and H. Vehkamaki, J. Geophys. Res. Atm. **110**, D06207 (2005). doi:06210.01029/02004jd005400.
[104] R.J. Hopkins, Y. Desyaterik, A.V. Tivanski, R.A. Zaveri, C.M. Berkowitz, T. Tyliszczak, M.K. Gilles, and A. Laskin, J. Geophys. Res. Atm. **113**, D04209 (2008). doi:04210.01029/02007jd008954.)
[105] Y. Liu, Z. Yang, Y. Desyaterik, P.L. Gassman, H. Wang, and A. Laskin, Anal. Chem. **80**, 633 (2008).
[106] Y. Liu, B. Minofar, Y. Desyaterik, E. Dames, Z. Zhu, J.P. Cain, R.J. Hopkins, M.K. Gilles, H. Wang, P. Jungwirth, and A. Laskin, PCCP **13**, 11846 (2011).
[107] R. von Glasow and P.J. Crutzen, Atmos. Chem. Phys. **4**, 589 (2004).
[108] G.B. Ellison, A.F. Tuck, and V. Vaida, J. Geophys. Res. Atm. **104**, 11633 (1999).
[109] Y. Rudich, Chem. Rev. **103**, 5097 (2003).
[110] T. Sakamoto, M. Koizumi, J. Kawasaki, and J. Yamaguchi, Appl. Surf. Sci. **255**, 1617 (2008).
[111] J.S. Fletcher, S. Rabbani, A. Henderson, P. Blenkinsopp, S.P. Thompson, N.P. Lockyer, and J. C. Vickerman, Anal. Chem. **80**, 9058 (2008).
[112] A. Carado, M.K. Passarelli, J. Kozole, J.E. Wingate, N. Winograd, and A.V. Loboda, Anal. Chem. **80**, 7921 (2008).
[113] Y. Kalegowda and S.L. Harmer, Anal. Chem. **84**, 2754 (2012).
[114] J.L. Guerquin-Kern, T.D. Wu, C. Quintana, and A. Croisy, Biochim. Biophys. Acta-Gen. Subj. **1724**, 228 (2005).
[115] S.G. Boxer, M.L. Kraft, and P.K. Weber, Ann. Rev. Biophys. **38**, 53 (2009).
[116] K. Heister, C. Hoschen, G.J. Pronk, C.W. Mueller, and I. Kogel-Knabner, J. Soils Sediments **12**, 35 (2012).
[117] A.M. Herrmann, K. Ritz, N. Nunan, P.L. Clode, J. Pett-Ridge, M.R. Kilburn, D.V. Murphy, A.G. O'Donnell, and E.A. Stockdale, Soil Biol. Biochem. **39**, 1835 (2007).
[118] L. Remusat, P.J. Hatton, P.S. Nico, B. Zeller, M. Kleber, and D. Derrien, Environ. Sci. Technol. **46**, 3943 (2012).
[119] T. Rennert, K.U. Totsche, K. Heister, M. Kersten, and J. Thieme, J. Soils Sediments **12**, 3 (2012).
[120] T.M. McIntire, O.S. Ryder, P.L. Gassman, Z. Zhu, S. Ghosal, and B.J. Finlayson-Pitts, Atmos. Environ. **44**, 939 (2010).
[121] B. Winterholler, P. Hoppe, S. Foley, and M.O. Andreae, Int. J. Mass Spectrom. **272**, 63 (2008).
[122] E. Harris, B. Sinha, S. Foley, J.N. Crowley, S. Borrmann, and P. Hoppe, Atmos. Chem. Phys. **12**, 4867 (2012).
[123] E. Harris, B. Sinha, P. Hoppe, J.N. Crowley, S. Ono, and S. Foley, Atmos. Chem. Phys. **12**, 407 (2012).
[124] J. Langner and H. Rodhe, J. Atmos. Chem. **13**, 225 (1991).
[125] M.H. Thiemens, Annu. Rev. Earth Planetary Sci. **34**, 217 (2006).
[126] B.J. Tyler, S. Dambach, S. Galla, R.E. Peterson, and H.F. Arlinghaus, Anal. Chem. **84**, 76 (2012).
[127] R.E. Peterson, A. Nair, S. Dambach, H.F. Arlinghaus, and B.J. Tyler, Appl. Surf. Sci. **252**, 7006 (2006).
[128] S. Ebata, M. Ishihara, K. Uchino, S. Itose, M. Matsuya, M. Kudo, K. Bajo, and H. Yurimoto, Surf. Interface Anal. **44**, 635 (2012).
[129] L.K. Takahashi, J. Zhou, K.R. Wilson, S.R. Leone, and M. Ahmed, J. Phys. Chem. A **113**, 4035 (2009).
[130] L.K. Takahashi, J. Zhou, O. Kostko, A. Golan, S.R. Leone, and M. Ahmed, J. Phys. Chem. A **115**, 3279 (2011).
[131] S.R. Leone, M. Ahmed, and K.R. Wilson, PCCP **12**, 6564 (2010).

[132] G. Pan, C.J. Hu, Z.Y. Wang, Y. Cheng, X.H. Zheng, X.J. Gu, W.X. Zhao, W.J. Zhang, J. Chen, F.Y. Liu, X.B. Shan, and L.S. Sheng, Rapid Commun. Mass Spectrom. **26**, 189 (2012).
[133] W.Z. Fang, L. Gong, X.B. Shan, F.Y. Liu, Z.Y. Wang, and L.S. Sheng, Anal. Chem. **83**, 9024 (2011).
[134] W.Z. Fang, L. Gong, Q. Zhang, M.Q. Cao, Y.Q. Li, and L.S. Sheng, Environ. Sci. Technol. **46**, 3898 (2012).
[135] E. Gloaguen, E.R. Mysak, S.R. Leone, M. Ahmed, and K.R. Wilson, Int. J. Mass Spectrom. **258**, 74 (2006).
[136] S.J. Hanna, P. Campuzano-Jost, E.A. Simpson, D.B. Robb, I. Burak, M.W. Blades, J.W. Hepburn, and A.K. Bertram, Int. J. Mass Spectrom. **279**, 134 (2009).
[137] S.J. Hanna, P. Campuzano-Jost, E.A. Simpson, I. Burak, M.W. Blades, J.W. Hepburn, and A. K. Bertram, PCCP **11**, 7963 (2009).
[138] E.A. Simpson, P. Campuzano-Jost, S.J. Hanna, K.M.M. Kanan, J.W. Hepburn, M.W. Blades, and A.K. Bertram, PCCP **12**, 11565 (2010).
[139] S. Geddes, B. Nichols, K. Todd, J. Zahardis, and G.A. Petrucci, Atmos. Measure. Tech. **3**, 1175 (2010).
[140] R.E. Russo, X.L. Mao, C. Liu, and J. Gonzalez, J. Anal. Atm. Spectrom. **19**, 1084 (2004).
[141] F. Aubriet and V. Carre, Anal. Chim. Acta **659**, 34 (2010).
[142] P. Lorazo, L.J. Lewis, and M. Meunier, Phys. Rev. Lett. **91**, 225502 (2003).
[143] L.V. Zhigilei, E. Leveugle, B.J. Garrison, Y.G. Yingling, and M.I. Zeifman, Chem. Rev. **103**, 321 (2003).
[144] C.A. Heinrich, T. Pettke, W.E. Halter, M. Aigner-Torres, A. Audetat, D. Gunther, B. Hattendorf, D. Bleiner, M. Guillong, and I. Horn, Geochim. Cosmochim. Acta **67**, 3473 (2003).
[145] G. Steinhoefel, J. Breuer, F. von Blanckenburg, I. Horn, D. Kaczorek, and M. Sommer, Chem. Geol. **286**, 280 (2011).
[146] F. Pointurier, A.C. Pottin, and A. Hubert, Anal. Chem. **83**, 7841 (2011).
[147] Z. Abrego, A. Ugarte, N. Unceta, A. Fernandez-Isla, M.A. Goicolea, and R.J. Barrio, Anal. Chem. **84**, 2402 (2012).
[148] B. Fernandez, F. Claverie, C. Pecheyran, and O.F.X. Donard, TrAC, Trends Anal. Chem. **26**, 951 (2007).
[149] J. Koch, S. Heiroth, T. Lippert, and D. Gunther, Spectroc. Acta Pt. B-Atom. Spectr. **65**, 943 (2010).
[150] L.A. Zhu, J. Stadler, T.A. Schmitz, F. Krumeich, and R. Zenobi, J. Phys. Chem. C **115**, 1006 (2011).
[151] J.A. Bradshaw, O.S. Ovchinnikova, K.A. Meyer, and D.E. Goeringer, Rapid Commun. Mass Spectrom. **23**, 3781 (2009).
[152] K.A. Meyer, O. Ovchinnikova, K. Ng, and D.E. Goeringer, Rev. Sci. Instrum. **79** (2008).
[153] T.A. Schmitz, G. Gamez, P.D. Setz, L. Zhu, and R. Zenobi, Anal. Chem. **80**, 6537 (2008).
[154] J. Cheng, A. Wucher, and N. Winograd, J. Phys. Chem. B **110**, 8329 (2006).
[155] P. Konarski, J. Haluszka, and M. Cwil, Appl. Surf. Sci. **252**, 7010 (2006).
[156] P. Konarski, K. Kaczorek, B. Balcerzak, J. Haluszka, M. Scibor, I. Iwanejko, and A. Zawada, Surf. Interface Anal. **43**, 470 (2011).
[157] A. Delcorte and B.J. Garrison, Nucl. Instrum. Methods Phys. Res. Sec. B **180**, 37 (2001).
[158] A. Delcorte and B.J. Garrison, J. Phys. Chem. B **104**, 6785 (2000).
[159] A. Delcorte, X. Vanden Eynde, P. Bertrand, J.C. Vickerman, and B.J. Garrison, J. Phys. Chem. B **104**, 2673 (2000).
[160] B.J. Garrison, A. Delcorte, and K.D. Krantzman, Accounts Chem. Res. **33**, 69 (2000).
[161] G. Friedbacher and H. Bubert, *Surface and Thin Film Analysis* (Wiley-VCH, Weinheim, 2011).
[162] N. Winograd and B.J. Garrison, Annu. Rev. Phys. Chem. **61**, 305 (2010).
[163] C.M. Mahoney, Mass Spectrom. Rev. **29**, 247 (2010).

[164] Z. Postawa, B. Czerwinski, M. Szewczyk, E.J. Smiley, N. Winograd, and B.J. Garrison, Anal. Chem. **75**, 4402 (2003).
[165] S. Rabbani, A.M. Barber, J.S. Fletcher, N.P. Lockyer, and J.C. Vickerman, Anal. Chem. **83**, 3793 (2011).
[166] T.T. Jarvi, J.A. Pakarinen, A. Kuronen, and K. Nordlund, *Epl* **82** (2008).
[167] L. Yang, M.P. Seah, E.H. Anstis, I.S. Gilmore, and J.L.S. Lee, J. Phys. Chem. C **116**, 9311 (2012).
[168] J.T. Shelley, S.J. Ray, and G.M. Hieftje, Anal. Chem. **80**, 8308 (2008).
[169] R. Valledor, J. Pisonero, N. Bordel, J.I. Martin, C. Quiros, A. Tempez, and A. Sanz-Medel, Anal. Bioanal. Chem. **396**, 2881 (2010).
[170] R. Valledor, J. Pisonero, T. Nelis, and N. Bordel, J. Anal. Atm. Spectrom. **26**, 758 (2011).
[171] Z. Xing, J.A. Wang, G.J. Han, B. Kuermaiti, S.C. Zhang, and X.R. Zhang, Anal. Chem. **82**, 5872 (2010).
[172] E. Woods, G.D. Smith, R.E. Miller, and T. Baer, Anal. Chem. **74**, 1642 (2002).
[173] T.D. Vaden, C. Song, R.A. Zaveri, D. Imre, and A. Zelenyuk, Proc. Natl. Acad. Sci. **107**, 6658 (2010).
[174] A. Zelenyuk, J. Yang, C. Song, R.A. Zaveri, and D. Imre, J. Phys. Chem. A **112**, 669 (2008).
[175] P. Kebarle and U.H. Verkerk, in *Electrospray and MALDI Mass Spectrometry: Fundamentals, Instrumentation, Practicalities, and Biological Applications*, edited by R.B. Cole (John Wiley & Sons, Hoboken, NJ, 2010), pp. 3–48.
[176] G. Taylor, Proc Roy. Soc. Lond. Ser. A **280**, 383 (1964).
[177] K. Tang and R.D. Smith, J. Am. Soc. Mass. Spectrom. **12**, 343 (2001).
[178] A.C. MacMillan, J.B. Morrison, C.W. Harmon, and S.A. Nizkorodov, Aerosol Sci. Technol. 1239 (2012).
[179] R.L. Grimm, R. Hodyss, and J.L. Beauchamp, Anal. Chem. **78**, 3800 (2006).
[180] H.I. Kim, H. Kim, Y.S. Shin, L.W. Beegle, W.A. Goddard, J.R. Heath, I. Kanik, and J.L. Beauchamp, J. Phys. Chem. B **114**, 9496 (2010).
[181] J.Y. Ko, S.M. Choi, Y.M. Rhee, J.L. Beauchamp, and H.I. Kim, J. Am. Soc. Mass. Spectrom. **23**, 141 (2012).
[182] E.E. Dodd, J. Appl. Phys. **24**, 73 (1953).
[183] S. Enami, M.R. Hoffmann, and A.J. Colussi, J. Phys. Chem. Lett. **1**, 1599 (2010).
[184] S. Enami, M.R. Hoffmann, and A.J. Colussi, J. Phys. Chem. B **112**, 4153 (2008).
[185] S. Enami, M.R. Hoffmann, and A.J. Colussi, Proc. Natl. Acad. Sci. **105**, 7365 (2008).
[186] S.Enami, M.R. Hoffmann, and A.J. Colussi, J. Phys. Chem. A **113**, 7002 (2009).
[187] S. Enami, M.R. Hoffmann, and A.J. Colussi, Chem. Res. Toxicol. **22**, 35 (2009).
[188] S. Enami, M.R. Hoffmann, and A.J. Colussi, J. Phys. Chem. A **114**, 5817 (2010).
[189] S. Enami, M.R. Hoffmann, and A.J. Colussi, J. Phys. Chem. Lett. **1**, 2374 (2010).
[190] S. Enami, H. Mishra, M.R. Hoffmann, and A.J. Colussi, J. Phys. Chem. A **116**, 6027 (2012).
[191] S. Enami, L.A. Stewart, M.R. Hoffmann, and A.J. Colussi, J. Phys. Chem. Lett. **1**, 3488 (2010).
[192] S. Enami, C.D. Vecitis, J. Cheng, M.R. Hoffmann, and A.J. Colussi, J. Phys. Chem. A **111**, 8749 (2007).
[193] S. Enami, C.D. Vecitis, J. Cheng, M.R. Hoffmann, and A.J. Colussi, Chem. Phys. Lett. **455**, 316 (2008).
[194] S. Hayase, A. Yabushita, M. Kawasaki, S. Enami, M.R. Hoffmann, and A.J. Colussi, J. Phys. Chem. A **114**, 6016 (2010).
[195] T. Kinugawa, S. Enami, A. Yabushita, M. Kawasaki, M.R. Hoffmann, and A.J. Colussi, PCCP **13**, 5144 (2011).
[196] H. Mishra, S. Enami, R.J. Nielsen, M.R. Hoffmann, W.A. Goddard, III, and A.J. Colussi, Proc. Natl. Acad. Sci. **109**, 10228 (2012).

[197] B.J. Finlayson-Pitts, Chem. Rev. **103**, 4801 (2003).
[198] E.M. Knipping, M.J. Lakin, K.L. Foster, P. Jungwirth, D.J. Tobias, R.B. Gerber, D. Dabdub, and B.J. Finlayson-Pitts, Science **288**, 301 (2000).
[199] B.M. Connelly and M.A. Tolbert, Environ. Sci. Technol. **44**, 4603 (2010).
[200] M.S. Westphall, K. Jorabchi, and L.M. Smith, Anal. Chem. **80**, 5847 (2008).
[201] K. Jorabchi and L.M. Smith, Anal. Chem. **81**, 9682 (2009).
[202] G.A. Eiceman and Z. Karpas, *Ion Mobility Spectrometry*. 2nd ed. (CRC Press, Taylor & Francis Group, Boca Raton, FL, 2005).
[203] A.B. Kanu, P. Dwivedi, M. Tam, L. Matz, and H.H. Hill, J. Mass Spectrom. **43**, 1 (2008).
[204] D.E. Clemmer and M.F. Jarrold, J. Mass Spectrom. **32**, 577 (1997).
[205] R.C. Flagan, Aerosol Sci. Technol. **28**, 301 (1998).
[206] S. Guha, M.D. Li, M.J. Tarlov, and M.R. Zachariah, Trends Biotechnol. **30**, 291 (2012).
[207] J. Rus, D. Moro, J.A. Sillero, J. Royuela, A. Casado, F. Estevez-Molinero, and J.F. de la Mora, Int. J. Mass Spectrom. **298**, 30 (2010).
[208] J. Christopher, Jr. and J.F. de la Mora, PCCP **11**, 8079 (2009).
[209] C.J. Hogan and J.F. de la Mora, J. Am. Soc. Mass. Spectrom. **21**, 1382 (2010).
[210] C. Larriba, C.J. Hogan, Jr., M. Attoui, R. Borrajo, J.F. Garcia, and J.F. de la Mora, Aerosol Sci. Technol. **45**, 453 (2011).
[211] B.K. Ku and J.F. de la Mora, Aerosol, Sci. Technol. **43**, 241 (2009).
[212] C.J. Koh, C.L. Liu, C.W. Harmon, D. Strasser, A. Golan, O. Kostko, S.D. Chambreau, G.L. Vaghjiani, and S.R. Leone, J. Phys. Chem. A **115**, 4630 (2011).
[213] D.J. Rader and P.H. McMurry, J. Aerosol Sci. **17**, 771 (1986).
[214] B. Gologan, J.M. Wiseman, and R.G. Cooks, in *Principles of Mass Spectrometry Applied to Biomolecules*, edited by J. Laskin and C. Lifshitz (John Wiley & Sons, Hoboken, NJ, 2006).
[215] G.E. Johnson, Q.C. Hu, and J. Laskin, Annu. Rev. Anal. Chem. **4**, 83 (2011).
[216] G. Verbeck, W. Hoffmann, and B. Walton, Analyst **137**, 4393 (2012).
[217] N.D. Loh, C.Y. Hampton, A.V. Martin, D. Starodub, R.G. Sierra, A. Barty, A. Aquila, J. Schulz, L. Lomb, J. Steinbrener, R.L. Shoeman, S. Kassemeyer, C. Bostedt, J. Bozek, S.W. Epp, B. Erk, R. Hartmann, D. Rolles, A. Rudenko, B. Rudek, L. Foucar, N. Kimmel, G. Weidenspointner, G. Hauser, P. Holl, E. Pedersoli, M. Liang, M.M. Hunter, L. Gumprecht, N. Coppola, C. Wunderer, H. Graafsma, F.R.N.C. Maia, T. Ekeberg, M. Hantke, H. Fleckenstein, H. Hirsemann, K. Nass, T.A. White, H.J. Tobias, G.R. Farquar, W.H. Benner, S.P. Hau-Riege, C. Reich, A. Hartmann, H. Soltau, S. Marchesini, S. Bajt, M. Barthelmess, P. Bucksbaum, K.O. Hodgson, L. Struder, J. Ullrich, M. Frank, I. Schlichting, H.N. Chapman, and M.J. Bogan, Nature **486**, 513 (2012).